RESEARCH ARTICLE | AUGUST 21 2024

Statistical evaluation of electric field distributions in 3D composites with a random spatial distribution of dielectric inclusions

Tobias Weber ; Romanus Dyczij-Edlinger ; Rolf Pelster

J. Appl. Phys. 136, 075103 (2024)
https://doi.org/10.1063/5.0217298

Journal of Applied Physics ARTICLE pubs.aip.org/aip/jap

Statistical evaluation of electric field distributions in 3D composites with a random spatial distribution of dielectric inclusions

Cite as: J. Appl. Phys. **136**, 075103 (2024); doi: 10.1063/5.0217298
Submitted: 3 May 2024 · Accepted: 2 August 2024 ·
Published Online: 21 August 2024

Tobias Weber,[1] Romanus Dyczij-Edlinger,[2] and Rolf Pelster[1,a)]

AFFILIATIONS

[1]Department of Physics, Saarland University, Campus E2.6, 66123 Saarbrücken, Germany
[2]Department of Systems Engineering, Saarland University, Campus C6.3, 66123 Saarbrücken, Germany

[a)]**Author to whom correspondence should be addressed:** rolf.pelster@mx.uni-saarland.de

ABSTRACT

Electromagnetic applications of composites often impose constraints on the internal electric fields, such as an upper limit on the field strength to prevent local heating or dielectric breakthrough. However, owing to heterogeneity, the local fields in a composite differ from those in a homogeneous material. Moreover, they are accessible neither by experiment nor by effective medium theories, at least for arbitrary microstructures. In this work, we use numerical simulations to evaluate the electric field distribution and the effective permittivity for 3D systems of monodisperse impenetrable spheres dispersed in a continuous matrix phase. We restrict ourselves to loss-free dielectric materials and to a random spatial distribution of particles. Samples are placed in a parallel plate waveguide and exposed to a transverse electromagnetic wave. The local field amplitudes are calculated via the finite element method and are normalized to those of a homogeneous sample exhibiting the same effective permittivity and geometry. We analyze the distribution of the local electric field strength in both constituents, namely, particles and matrix. Thus, we evaluate mean values and standard deviations as well as the field strengths characterizing the highest and lowest percentiles. Increasing particle concentration or permittivity enhances heterogeneity, and so the local electric field strength in some domains can become much higher than its average value. The methods we apply here can also be used in further investigations of more complex systems, including lossy materials and agglomerating particles.

I. INTRODUCTION

Composites consisting of nanosized particles embedded in a host matrix are of great interest for the development of new electromagnetic materials with tailored properties. Their fields of application include, for example, shielding or absorption of electromagnetic waves, cloaking, antennas, and sensors for structural health monitoring.[1] For example, the ferromagnetic resonance of a material can shift significantly when it is embedded in the form of inclusions in a nonmagnetic environment,[2] and such materials can serve as absorbers over a wide frequency range.[3] Moreover, with regard to electrical energy storage, composites with enhanced permittivity due to the presence of embedded dielectric particles may be superior to homogeneous dielectrics.[4] However, in electromagnetic applications, heterogeneity also leads to spatial fluctuations of internal fields. "High-field spots" or "hot spots," i.e., areas of very high electric field strength or high generation of Joule heat, represent a possible drawback.[5,6] To cite an example, for moderate thermal heating of a biological system via high-frequency radiation—as in diathermy in medicine—damage due to excessively elevated local temperatures must be avoided.[7] An example of a numerical analysis of the field distribution in conducting tissue is given in Ref. 8. It is also important to take the field distribution into account when composite materials are used to construct electronic devices such as capacitors, where the need to prevent electrical breakdown imposes an upper limit on the electric field strength.[9] Field distributions and corresponding probability density functions can be evaluated numerically: examples in the case of 2D systems can be found in Ref. 10 (randomly dispersed disks, squares, or needles) and in Ref. 11 (periodic and random arrays of cylinders). Analytical bounds on

field fluctuations in 2D and 3D systems, i.e., on the variance of the electric field strength, have been derived in Refs. 12 and 13.

In the present work, we evaluate and analyze the electric field distributions in both constituents of 3D binary composites. For this purpose, we use finite element simulations and consider monodisperse spherical inclusions in a continuous matrix (the so-called cermet topology). We restrict ourselves to a model system of dielectric materials with no losses and to spatially random distributions of non-overlapping particles. To understand and to quantify the effects of heterogeneity, we investigate the influence of increasing dielectric contrast and particle concentration on the field distribution.

II. FUNDAMENTALS: EFFECTIVE PERMITTIVITY AND MEAN VALUES OF THE ELECTRIC FIELD AMPLITUDE

The effective permittivity of a heterogeneous material is related to the spatially averaged mean values of the field distributions in its constituents (in our case, matrix and particles). This holds not only in static fields but also for the propagation of electromagnetic waves, as long as the wavelength λ is large compared with the length scale of the inhomogeneities. In our case, this effective medium condition is $\lambda \gg r_{\mathrm{inc}}$, where r_{inc} denotes the radius of the dispersed spheres. In the following, we recall the relevant theoretical foundations, which can be found in many textbooks (see, e.g., Refs. 14–17). For this purpose, we consider a time-harmonic electromagnetic wave traveling in the z direction. This may be a transverse electromagnetic wave (TEM mode or plane wave) or a transverse electric wave (TE mode) in a rectangular waveguide. For propagation in a homogeneous (nonmagnetic) dielectric medium extending infinitely in the z direction, the electric field at the position vector $\mathbf{r}$ can be written as

$$\mathbf{E}_{\mathrm{hom}}(\mathbf{r}, t) = \mathbf{E}_{0,\mathrm{hom}}(\mathbf{r}) e^{-i(k'z-\omega t+\phi)}, \tag{1}$$

where ω is the angular frequency, c is the speed of light, t is the time, and ϕ is a phase shift. The complex wavenumber $k = k' - ik'' = (\omega/c)\sqrt{\varepsilon_{\mathrm{hom}}}$ depends on the relative permittivity $\varepsilon_{\mathrm{hom}} = \varepsilon'_{\mathrm{hom}} - i\varepsilon''_{\mathrm{hom}}$ of the medium (k', k'', $\varepsilon'_{\mathrm{hom}}$, $\varepsilon''_{\mathrm{hom}} \geq 0$). Equivalently, an alternative time-harmonic convention can be adopted with the opposite sign of the argument in the exponential function.[18] For an oscillation in the y–z plane (see the blue curve in Fig. 1), the field amplitude is given by

$$\mathbf{E}_{0,\mathrm{hom}}(\mathbf{r}) = \begin{pmatrix} 0 \\ A_{0,\mathrm{hom}}(\mathbf{r}) \\ 0 \end{pmatrix} e^{-k''z} \quad \in \mathbb{R}^3. \tag{2}$$

For a TEM mode in a loss-free medium, i.e., for $\varepsilon''_{\mathrm{hom}} = 0$ and, thus, $k'' = 0$, $E_{0,\mathrm{hom},y}$ is spatially constant, and the same holds when the material is placed in a parallel plate capacitor and exposed to a static field [the real part of Eq. (1) with $\omega = 0$ and $\phi = 0$]. In contrast, a wave propagating in a lossy medium dissipates energy and is attenuated, and so $E_{0,\mathrm{hom},y} \propto \exp(-k''z)$ decreases as a function of z, but it is independent of x and y in the case of a TEM mode.

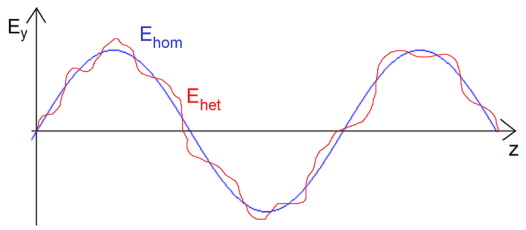

FIG. 1. Electric field of a TEM mode propagating in the z direction for a loss-free composite of permittivity $\varepsilon_{\mathrm{eff}}$ [red curve, real part of Eq. (3) for $t = 0$ and $\phi = \pi/4$] compared with that in a homogeneous medium of the same permittivity [blue curve; see Eq. (1)]. The wavevectors are identical and, thus, also the wavelengths. In the composite, however, local inhomogeneities perturb the sinusoidal shape, i.e., the modulus and orientation of the local field amplitude $\mathbf{E}_0(\mathbf{r})$ fluctuate around those for the effective homogeneous medium [see Eqs. (2) and (4)–(6)].

In a heterogeneous system (in which the effective medium condition holds), wave propagation is similar, i.e.,

$$\mathbf{E}_{\mathrm{het}}(\mathbf{r}, t) = \mathbf{E}_0(\mathbf{r}) e^{-i(k'_{\mathrm{eff}}z-\omega t+\phi)} \tag{3}$$

holds, where $k_{\mathrm{eff}} = (\omega/c)\sqrt{\varepsilon_{\mathrm{eff}}}$ denotes the effective wavenumber, with $\varepsilon_{\mathrm{eff}} = \varepsilon'_{\mathrm{eff}} - i\varepsilon''_{\mathrm{eff}}$ being the relative effective permittivity of the composite. But here, the modulus and the orientation of the field amplitude,

$$\mathbf{E}_0(\mathbf{r}) = \begin{pmatrix} A_{0,x}(\mathbf{r}) \\ A_{0,y}(\mathbf{r}) \\ A_{0,z}(\mathbf{r}) \end{pmatrix} e^{-k''_{\mathrm{eff}}z} \quad \in \mathbb{C}^3, \tag{4}$$

exhibit spatial fluctuations on the length scale of the inhomogeneities. Apart from these local fluctuations, wave propagation in the heterogeneous material corresponds to that in a homogeneous material of permittivity $\varepsilon_{\mathrm{hom}} = \varepsilon_{\mathrm{eff}}$, i.e., on average, the field amplitudes are equal (compare the red and blue curves in Fig. 1). This can be put into a mathematical form defining the normalized field amplitude in the heterogeneous composite,

$$\mathbf{E}_{\mathrm{norm}}(\mathbf{r}) = \frac{\mathbf{E}_0(\mathbf{r})}{\left(E_{0,\mathrm{hom},y}(\mathbf{r})\right)_{\varepsilon_{\mathrm{hom}}=\varepsilon_{\mathrm{eff}}}}, \tag{5}$$

with a spatially averaged mean value,

$$\langle \mathbf{E}_{\mathrm{norm}} \rangle = \begin{pmatrix} 0 \\ 1 \\ 0 \end{pmatrix}, \tag{6}$$

where the brackets $\langle \cdots \rangle$ denote the volume average $V^{-1} \int \cdots dV$. Although heterogeneities in the composite can induce components of $\mathbf{E}_0(\mathbf{r})$ in the x and z directions [see Eq. (4)], these vanish on average. However, they do contribute to the mean field strength, i.e., to the average modulus of the field amplitude, and so $\langle |\mathbf{E}_{\mathrm{norm}}| \rangle \geq 1$ holds. The above procedure also applies in the case of

magnetic composites, where the wave vector additionally depends on the effective permeability.[19]

Next, we relate the effective permittivity ε_{eff} to the normalized average fields in the constituents of the composite, in our case matrix and particles.[20,21] This line of reasoning is not restricted to wave propagation in infinite media. It also applies to a superposition of waves, which may occur owing to multiple reflections between the front and the back side of a finite sample, or to static fields. The local field amplitude of the dielectric displacement in a composite is given by

$$\mathbf{D}_0(\mathbf{r}) = \varepsilon_0 \varepsilon(\mathbf{r}) \mathbf{E}_0(\mathbf{r}), \tag{7}$$

with ε_0 being the permittivity of the vacuum and $\varepsilon(\mathbf{r})$ being the local permittivity [$\varepsilon(\mathbf{r}) = \varepsilon_p$ in particles and $\varepsilon(\mathbf{r}) = \varepsilon_m$ in the matrix]. On the other hand, its spatial average

$$\langle \mathbf{D}_0 \rangle = \varepsilon_0 \varepsilon_{\text{eff}} \langle \mathbf{E}_0(\mathbf{r}) \rangle \tag{8}$$

is related to the effective permittivity. Rewriting Eqs. (7) and (8) for the normalized fields [see Eqs. (5) and (6)] and combining the right-hand sides yield

$$\begin{aligned} \begin{pmatrix} 0 \\ \varepsilon_{\text{eff}} \\ 0 \end{pmatrix} &= \langle \varepsilon(\mathbf{r}) \mathbf{E}_{\text{norm}}(\mathbf{r}) \rangle \\ &= f \varepsilon_p \langle \mathbf{E}_{\text{norm}}(\mathbf{r}) \rangle_p + (1-f) \varepsilon_m \langle \mathbf{E}_{\text{norm}}(\mathbf{r}) \rangle_m. \end{aligned} \tag{9}$$

The brackets $\langle \cdots \rangle_i = V_i^{-1} \int \cdots dV_i$ denote the spatial mean value in the corresponding constituent of volume V_i, with $i = m, p$ (the total volume of the composite, $V = V_p + V_m$, is the sum of the volume of the particles, V_p, and that of the matrix, V_m). $f = V_p/V$ denotes the volume filling factor of the particles ($f \in [0, 1]$), and accordingly, $1 - f = V_m/V$ is the volume fraction of the matrix. Likewise, the mean normalized field amplitude $\langle \mathbf{E}_{\text{norm}} \rangle$ [see Eq. (6)] can be written in terms of the mean values in its constituents,

$$\begin{pmatrix} 0 \\ 1 \\ 0 \end{pmatrix} = f \langle \mathbf{E}_{\text{norm}}(\mathbf{r}) \rangle_p + (1-f) \langle \mathbf{E}_{\text{norm}}(\mathbf{r}) \rangle_m. \tag{10}$$

Equation (10) can be used *inter alia* for a consistency check of field distributions obtained via numerical simulations (see below). In addition, it illustrates the interdependence of the mean values of the field distribution in particles and matrix. Therefore, it allows us to eliminate either $\langle \mathbf{E}_{\text{norm}}(\mathbf{r}) \rangle_p$ or $\langle \mathbf{E}_{\text{norm}}(\mathbf{r}) \rangle_m$ in Eq. (9). In doing so, we obtain for the y component,

$$\langle E_{\text{norm},y} \rangle_p = \frac{1}{f} \frac{\varepsilon_{\text{eff}}/\varepsilon_m - 1}{\varepsilon_p/\varepsilon_m - 1}, \tag{11}$$

$$\langle E_{\text{norm},y} \rangle_m = \frac{1}{1-f} \frac{\varepsilon_p/\varepsilon_m - \varepsilon_{\text{eff}}/\varepsilon_m}{\varepsilon_p/\varepsilon_m - 1} \tag{12}$$

(see also Refs. 12, 22, and 23), while the x and z components vanish. In the case of lossy materials, the permittivities and, thus, the mean values of the field amplitudes in particles and matrix [cf. Eq. (4)] are complex quantities, i.e., there is a phase shift $\langle E_{\text{norm},y} \rangle_i = |\langle E_{\text{norm},y} \rangle_i| \exp(-i\Delta\phi_i)$, although the weighted sum equals unity [see Eq. (10)]. A value $|\langle E_{\text{norm},y} \rangle_p| > 1$ or $|\langle E_{\text{norm},y} \rangle_p| < 1$ indicates that the average field amplitude in the particles is higher or lower than that in a homogeneous material of permittivity ε_{eff}. An analogous relation holds for $\langle E_{\text{norm},y} \rangle_m$. Thus, we can experimentally evaluate the normalized mean field amplitude in particles and matrix by measuring ε_{eff}, provided that the material parameters ε_m and ε_p as well as the filling factor f are known. However, in the majority of cases, we will have no access to the local field amplitudes $\mathbf{E}_{\text{norm}}(\mathbf{r})$ and local field strengths $|\mathbf{E}_{\text{norm}}(\mathbf{r})|$ (those are only known *a priori* for very simple microstructures such as a stack of material sheets oriented parallel or perpendicular to the applied field).

On the other hand, numerical simulations of the local field amplitudes allow us to evaluate the effective permittivity. Rearranging Eq. (11) yields

$$\frac{\varepsilon_{\text{eff}}}{\varepsilon_m} = 1 + f \left(\frac{\varepsilon_p}{\varepsilon_m} - 1 \right) \langle E_{\text{norm},y} \rangle_p. \tag{13}$$

Note that the value of $\varepsilon_{\text{eff}}/\varepsilon_m$ depends not only on the dielectric ratio $\varepsilon_p/\varepsilon_m$ and the filling factor f but also on the geometrical arrangement of the constituents, i.e., in our case on the spatial distribution of the particles: a change in microstructure affects the average field amplitude $\langle E_{\text{norm}} \rangle_p$ and, thus, results in an altered effective permittivity. The spectral representation of the effective permittivity developed by Bergman, Fuchs, and Milton (for a review, see Ref. 24) manifests this dependence on microstructure explicitly. It can be illustrated, for example, via simulations of composites in which the dielectric ratio and filling factor are kept constant while the microstructure is varied[25] or in experiments on ferrofluids (colloidal dispersions of magnetic nanoparticles), where the formation and orientation of particle clusters can be tuned via an external static magnetic field.[26] As a consequence, the dependence of ε_{eff} on microstructure needs to be taken into account when experimental data are analyzed (see, e.g., Refs. 27– 29). For an example of a numerical study of effective permittivity of simple 2D and 3D composite materials considering averaged fields, we refer to Ref. 30. Of course, apart from field simulations, the effective permittivity can be computed via other methods. For example, there are analytical formulas for monodisperse spheres on a cubic lattice[31,32] and an analytical exact solution for an arbitrary spatial configuration of spherical inclusions.[33,34]

In summary, the effective permittivity of a composite is related to the mean field amplitude in its constituents, and we shall come back to the fundamental Eqs. (10)–(13) when we discuss the results of our numerical simulations.

III. SIMULATION METHOD

We start with an outline of the procedure and give further details subsequently. First, we generate a composite with a given number N_{inc} of inclusions with permittivity ε_p that we insert randomly into a matrix (using uniformly distributed random numbers

to assign coordinates), respecting the exclusion principle (no overlap is allowed). Without loss of generality, we chose a matrix permittivity of $\varepsilon_m = 1$ (it is sufficient to vary ε_p and, thus, the dielectric ratio $\varepsilon_p/\varepsilon_m$; see Sec. II). As sketched in Fig. 2, the sample is placed in a parallel plate waveguide and exposed to an incident transverse electromagnetic wave (TEM mode). The numerical simulation is based on an H(curl) conforming finite element method[35] and yields the field amplitudes $\mathbf{E}_0(\mathbf{r}_i)$ at position vectors $\mathbf{r}_i$ inside the composite as well as the transmitted and reflected waves. The latter information is used to calculate the effective permittivity ε_{eff} of the composite. Subsequently, we repeat the simulation with a homogeneous sample of permittivity ε_{eff} having the same geometric extensions as the composite. In doing so, we determine the field amplitudes $\mathbf{E}_{0,\text{hom}}(\mathbf{r}_i)$ of the corresponding homogeneous effective medium. Note that these values are not constant but vary along the z axis owing to multiple reflections between the front and back sides. The data from both simulation runs allow us to calculate the normalized field amplitudes $\mathbf{E}_{\text{norm}}(\mathbf{r}_i)$ [see Eq. (5)].

We use the finite element method solver *Electronics Desktop 2019 R2* from Ansys[36] to model our composites and the experimental setup *in silico* and to calculate the electromagnetic fields. Figure 3 presents an example of an implementation showing the parallel plate waveguide with a composite sample. To obtain the propagation conditions for a TEM mode within a necessarily finite simulation volume, the left and right sidewalls, which are parallel to the z–y plane, are defined as perfect magnetic conductors, with the tangential magnetic field set to zero. The same boundary conditions may be realized by repeatedly adding images[37] of the randomly distributed particles to the sidewalls. Hence, in the model, the original particle configuration becomes the unit cell of a structure that is periodic along the x direction (perpendicular to the direction of propagation) on a length scale b that is a multiple of the mean distance between particles (see Fig. 3).[38] In the empty waveguide as well as in the waveguide filled with a homogeneous and loss-free sample, this leads to a constant field amplitude $\mathbf{E}_{0,\text{hom}} \propto \mathbf{e}_y$ (in contrast, electrically conductive sidewalls would impose field amplitudes that vanished for $x \to 0$ and $x \to b$). We choose a frequency $\nu = 1\,\text{GHz}$ corresponding to a wavelength $\lambda_0 = 30\,\text{cm}$ in the empty waveguide, changing to $\lambda = \lambda_0/\sqrt{\varepsilon_{\text{eff}}}$ inside the sample. Therefore, the effective medium condition $\lambda \gg r_{\text{inc}}$ is fulfilled in our simulations, where particle radii are limited to $r_{\text{inc}} \leq 0.0682$ cm, and $\varepsilon_{\text{eff}} < 1.25$ holds (see below, where we restrict ourselves to filling factors $f \leq 0.1$ and to dielectric ratios $\varepsilon_p/\varepsilon_m \leq 8$).

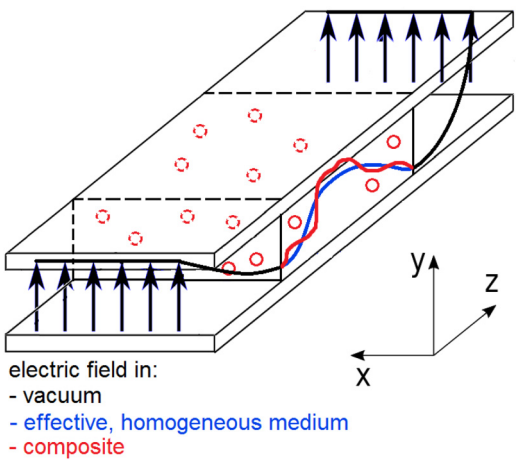

FIG. 2. Sketch of an ideal parallel plate waveguide with a sample (composite or the corresponding homogeneous effective medium). The upper and lower metallic plates extend infinitely in the x–z plane, and the extent of the sample is finite in the z direction but infinite in the x direction. An incident TEM wave with wavelength λ_0 and constant field amplitude propagates in the z direction through the empty waveguide before it reaches the sample. Inside the medium, its wavelength changes to $\lambda = \lambda_0/\sqrt{\varepsilon_{\text{eff}}}$. The discontinuities at the front and back sides lead to multiple partial reflections, and, therefore, even in the homogeneous case, the field amplitude in the sample varies as a function of z. Part of the incident wave is reflected and part is transmitted (see Fig. 4).

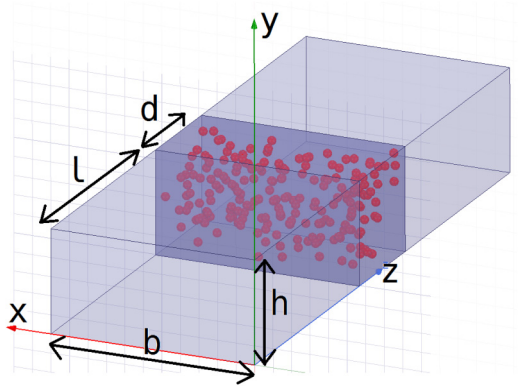

FIG. 3. Waveguide model as implemented in the simulation software. Geometric extensions of the waveguide and the device are chosen as $l = 2.5$ cm, $d = 1.1$ cm, $h = 1.1$ cm, and $b = 2.2$ cm. The upper and lower plates are defined as perfect electric conductors and the left and right sidewalls are defined as perfect magnetic conductors so that a TEM mode can propagate (cf. Fig. 2). In the configuration displayed, the composite contains $N_{\text{inc}} = 200$ spherical inclusions with a volume fraction $f = 0.01$, implying a radius $r_{\text{inc}} \simeq 0.0317$ cm.

The software generates a network of tetrahedra on which the Maxwell equations are discretized and solved. To enhance the accuracy, this first finite element mesh is further refined, i.e., locally adapted where a higher resolution is required (so-called refinement passes). The final mesh is not homogeneous, but we can extract the electric field amplitudes $\mathbf{E}_0$ or $\mathbf{E}_{0,\text{hom}}$ inside the sample at positions $\mathbf{r}_i$ on a simple cubic lattice of lattice constant a_{lat}. In this way, every field value is representative of a subvolume a_{lat}^3, i.e., the field amplitudes are equally weighted in the distributions that we evaluate. In Sec. IV, we determine the simulation parameters that are required to ensure a sufficient level of accuracy: the number of mesh passes (first discretization plus refinement passes), the number of particles N_{inc}, and the number of field amplitudes that we extract, $N_{\text{points}} \propto 1/a_{\text{lat}}^3$.

The effective permittivity ε_{eff} of a composite is determined by the transmission–reflection method (see Fig. 4). An incident wave,

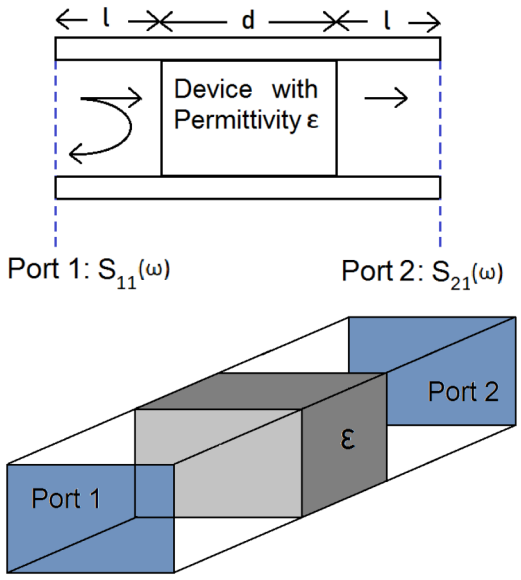

FIG. 4. Experimental setup for determining the permittivity of a sample using the transmission–reflection method (side view and perspective view). The incident wave propagates from left to right. Measuring the reflected and the transmitted waves at ports 1 and 2, respectively, allows us to determine the scattering parameters $S_{11}(\omega)$ and $S_{21}(\omega)$ and, thus, the permittivity.

$\mathbf{E}_{\text{inc}} \propto \mathbf{e}_y$ at port 1, travels a distance l along the empty waveguide in the z direction. Part is reflected and travels back to port 1, and another part is transmitted and travels a distance l forward to port 2. The so-called scattering parameters S_{11} and S_{21} relate the reflected wave at port 1 and the transmitted wave at port 2 to the incident wave at port 1,[40]

$$S_{11} = \frac{E_{\text{refl},y}}{E_{\text{inc},y}} = \frac{(1-a^2)r}{1-r^2a^2} e^{-ik_0 2l}, \tag{14}$$

$$S_{21} = \frac{E_{\text{trans},y}}{E_{\text{inc},y}} = \frac{(1-r^2)a}{1-r^2a^2} e^{-ik_0 2l}. \tag{15}$$

Here, $k_0 = 2\pi/\lambda_0 = \omega/c$ denotes the wavenumber of the empty waveguide, and so, $k_0 2l$ is the corresponding phase shift along a distance $2l$. For a nonmagnetic sample, the reflection coefficient at the interface between the empty and the filled waveguide,

$$r = \frac{1-\sqrt{\varepsilon_{\text{eff}}}}{1+\sqrt{\varepsilon_{\text{eff}}}}, \tag{16}$$

depends only on the effective permittivity.[39] The same holds for the propagation factor in the sample of length d, which is given by

$$a = \exp(-ik_{\text{eff}} d). \tag{17}$$

Equations (14) and (15) take multiple reflections of the TEM wave between the front and the back face of the sample into account. The simulation gives us access to the electric fields at both ports and, thus, to the respective scattering parameters. The effective permittivity of nonmagnetic composites can be determined numerically by solving Eq. (14) or Eq. (15). We use the analytical method developed by Nicholson and Ross,[40] and Weir,[40,41] combining Eqs. (14) and (15). Since the wavelength in the sample, $\lambda_0/\sqrt{\varepsilon_{\text{eff}}}$, is at least 24 times higher than the sample length d, which, in turn, is much higher than the interparticle distances, there are no resonance effects due to multiple reflections that might distort the retrieval of the effective permittivity.[42]

IV. ACCURACY ANALYSIS

In this section, we shall assess the accuracy of our simulations. For this purpose, we shall determine the number of particles N_{inc}, the number of mesh passes, and the number of field amplitudes N_{points} needed to obtain statistically reliable information about the variation of the local field strength $|\mathbf{E}_{\text{norm}}(\mathbf{r})|$ in a composite. To determine the frequency of occurrence of field values, we choose a high number $n+1$ of equidistant sampling points $|\mathbf{E}_{\text{norm},k}|$ $(k = 1, \ldots, n+1)$ defining sufficiently small intervals of width $\Delta|\mathbf{E}_{\text{norm}}|$ and evaluate for both the particle and matrix phases the number of field points $N_{k,i}$ $(i = p, m)$ with a field strength $|\mathbf{E}_{\text{norm},i}|$ in each of the n intervals $]|\mathbf{E}_{\text{norm},k}|, |\mathbf{E}_{\text{norm},k}| + \Delta|\mathbf{E}_{\text{norm}}|]$ (with $k = 1, \ldots, n$). Normalizing to the total number of field points $N_{\text{points},i}$ in the respective phase ($N_{\text{points}} = N_{\text{points},m} + N_{\text{points},p}$ holds) yields the histograms displayed in Figs. 5–7,

$$g_p(|\mathbf{E}_{\text{norm},k}|) = \frac{N_{k,p}}{N_{\text{points},p}}, \tag{18}$$

$$g_m(|\mathbf{E}_{\text{norm},k}|) = \frac{N_{k,m}}{N_{\text{points},m}}. \tag{19}$$

In the following, we shall refer to g_p and g_m as distributions of local electric field strengths. Note that the integrals $\int g_i\, d|\mathbf{E}_{\text{norm}}|$ are not normalized to one, i.e., g_p and g_m are proportional to but not equal to probability densities.

We start with a variation in the number of particles N_{inc}, keeping the other parameters fixed (see Fig. 5). More precisely, we use three mesh refinement passes and evaluate the field amplitudes at $N_{\text{points}} = 28\,224$ points on a simple cubic lattice with lattice constant $a_{\text{lat}} = 0.044$ cm, i.e., $24 \times 24 \times 49$ positions in a sample volume $V = dhb = 1.1 \times 1.1 \times 2.2\,\text{cm}^3$ (see Fig. 3). In addition, we choose a dielectric ratio $\varepsilon_p/\varepsilon_m = 5$ and a volume filling factor of $f = 0.1$. Since

$$f = \frac{V_p}{V} = N_{\text{inc}} \frac{4\pi}{3V} r_{\text{inc}}^3, \tag{20}$$

the particle radius r_{inc} has to be adapted when we vary the number of inclusions N_{inc} keeping f constant. In Fig. 5, we display the distribution of local field strengths $|\mathbf{E}_{\text{norm}}(\mathbf{r})|$ in particles and matrix for values from $N_{\text{inc}} = 10$ to $N_{\text{inc}} = 200$ with radii ranging from $r_{\text{inc}} \simeq 0.185$ cm down to $r_{\text{inc}} \simeq 0.068$ cm. The distributions for $N_{\text{inc}} = 10$ differ markedly from those at higher particle numbers.

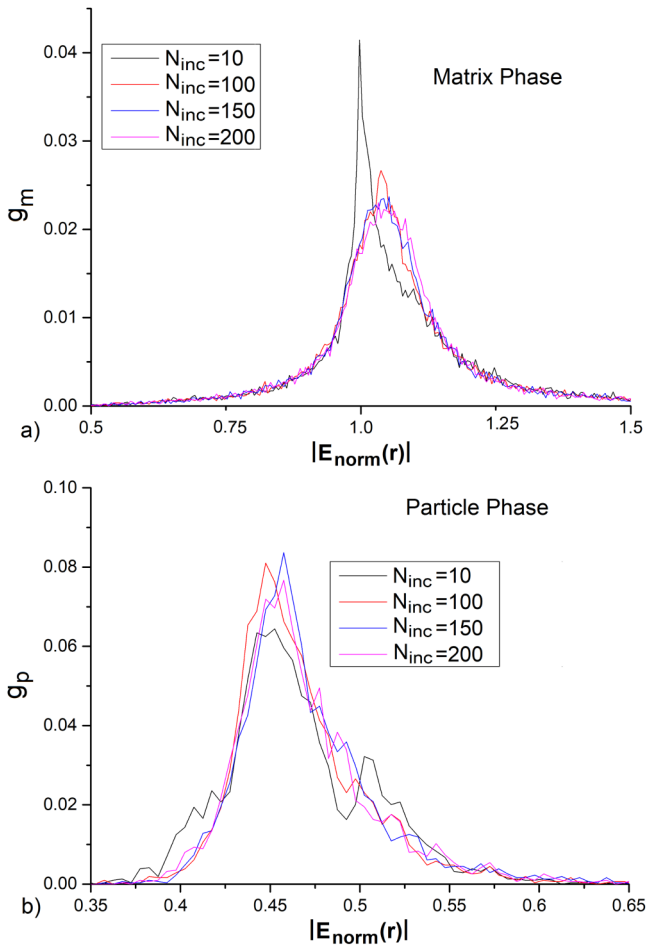

FIG. 5. Distributions of local electric field strengths $|\mathbf{E}_{\text{norm}}(\mathbf{r})|$ [cf. Eq. (5)] in matrix (a) and particles (b) for different inclusion numbers N_{inc}. The simulation's mesh generator performed three passes and we evaluated $N_{\text{points}} = 28\,224$ field points (lattice constant $a_{\text{lat}} = 0.044$ cm). The dielectric ratio was fixed at $\varepsilon_p/\varepsilon_m = 5$ and the volume filling factor at $f = 0.1$. According to Eq. (20), the particle radius changes with N_{inc}: $r_{\text{inc}} = 0.185$ cm for $N_{\text{inc}} = 10$, $r_{\text{inc}} = 0.086$ cm for $N_{\text{inc}} = 100$, $r_{\text{inc}} = 0.075$ cm for $N_{\text{inc}} = 150$, and $r_{\text{inc}} = 0.068$ cm for $N_{\text{inc}} = 200$.

In the matrix phase, the distributions show only marginal differences for $N_{\text{inc}} \geq 100$. The distributions also converge in the particle phase, but the data are still noisy. However, owing to a limited computing capacity, we are not able to further increase the number of inclusions. Thus, we shall use $N_{\text{inc}} = 200$ in the following and reduce statistical errors by averaging results over ten composites with different random spatial distributions of particles. Corresponding data will be marked with error bars indicating the standard deviation of the averaged data.

Next, we examine the influence of the number of mesh refinement passes. Figure 6 displays the corresponding distributions of field strengths. For the matrix, the distributions g_m obtained with one to three mesh passes are indistinguishable. In contrast, for the particle phase, the distribution g_p obtained with the first pass clearly differs from those obtained after one or two additional refinement passes. Since the particles constitute only 10% of the sample volume, the first finite element mesh is too coarse: the field strength $|\mathbf{E}_{\text{norm}}(\mathbf{r})|$ at positions close to the particle surface is obtained via an interpolation of the field strength at mesh points inside (lower field strength) and outside (higher field strength) the particles and, thus, is enhanced [cf. Figs. 6(a) and 6(b)].

Finally, we turn to the number N_{points} of field amplitudes on a simple cubic lattice required to obtain statistically reliable distributions of local field strengths $|\mathbf{E}_{\text{norm}}(\mathbf{r})|$ in the composite volume $V = dhb = 1.1 \times 1.1 \times 2.2\,\text{cm}^3$ (see Fig. 3). The results are displayed in Fig. 7. We observe that the distributions for $N_{\text{points}} = 5 \times 5 \times 10 = 250$ (lattice constant $a_{\text{lat}} = 0.2$ cm) are very blurred and deviate strongly from those for $N_{\text{points}} = 12 \times 12 \times 24 = 3456$ ($a_{\text{lat}} = 0.088$ cm) and $N_{\text{points}} = 24 \times 24 \times 49 = 28\,224$ ($a_{\text{lat}} = 0.044$ cm). The higher the value of N_{points}, the smoother is the distribution, but the shapes of the distributions converge for $N_{\text{points}} = 28\,224$.

In summary, we have shown empirically that the choice of $N_{\text{inc}} = 200$, three mesh passes, and $N_{\text{points}} = 28\,224$ ensures sufficient numerical convergence in our simulations.

In addition to convergence, we also want to assess the accuracy of our results. For this purpose, we compare the simulated effective permittivities with those from an analytically exact solution. For an arbitrary spatial configuration of spherical inclusions, Fu *et al.*[33] derived an equation for ε_{eff} that can be evaluated numerically, with the positions and sizes of all particles specified. In Ref. 43, it was shown that in the case of monodisperse spheres and for filling factors below the percolation threshold, the result corresponds to the analytical Maxwell–Garnett formula,[44–47]

$$\frac{\varepsilon_{\text{eff}}}{\varepsilon_m} = 1 + f\frac{\varepsilon_p/\varepsilon_m - 1}{1 + (1-f)(\varepsilon_p/\varepsilon_m - 1)/3}. \tag{21}$$

This result is exact only for spheres of identical size, and it is otherwise just a dilute limit approximation. In the case of polydisperse particles, higher permittivities are obtained, and for sufficiently broad particle size distributions, the effective permittivity approaches values corresponding to the Hanai–Bruggeman formula.[43] However, since the composites that we simulate consist of monodisperse spheres randomly dispersed in a continuous matrix, Eq. (21) does apply, and we shall use it as an analytical reference. We display this analytical prediction as a function of the dielectric contrast for different filling factors [curves in Fig. 8(a)] as well as a function of the filling factor for different dielectric ratios [curves in Fig. 8(b)]. The ε_{eff} values that we obtain numerically from the S parameters (see Sec. III) are very close to this reference. The accuracy decreases with increasing dielectric ratio or filling factor, and we observe a maximum deviation of 0.5% at $\varepsilon_p/\varepsilon_m = 8$ and $f = 0.1$.

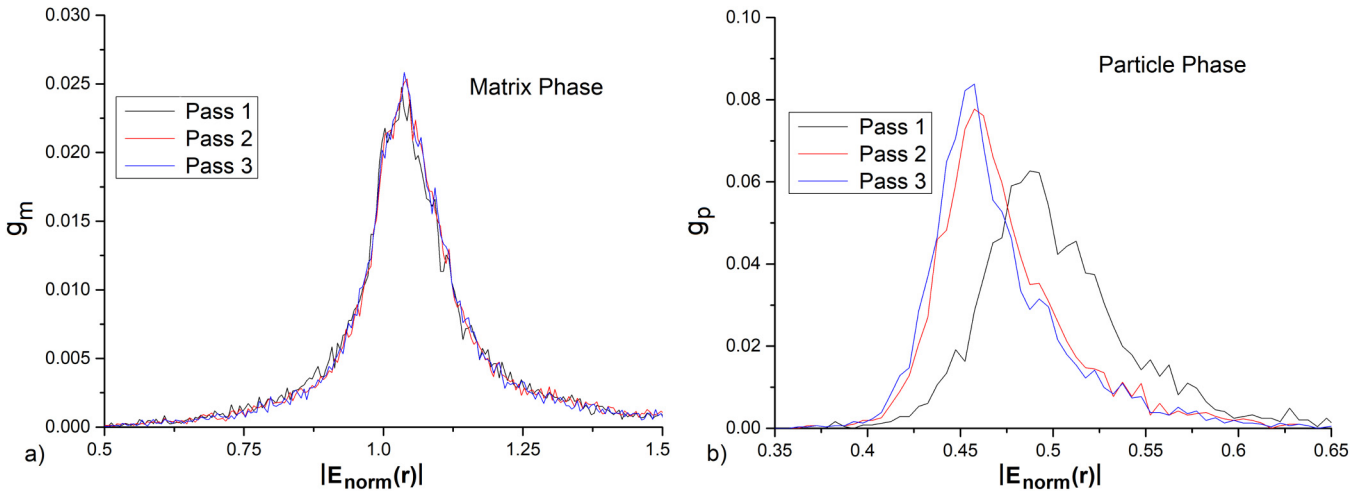

FIG. 6. Distributions of the local field strengths $|\mathbf{E}_{norm}(\mathbf{r})|$ in matrix (a) and particles (b) for increasing number of mesh passes yielding a refinement (increasing discretization levels of the software's default settings). Parameters were chosen as $f = 0.1$, $\varepsilon_p/\varepsilon_m = 5$, $N_{inc} = 200$ ($r = 0.068$ cm), and $N_{points} = 28\,224$ ($a_{lat} = 0.044$ cm).

V. ANALYZING THE DISTRIBUTIONS OF LOCAL ELECTRIC FIELD STRENGTHS

As already mentioned, the modulus and orientation of the normalized field amplitude $\mathbf{E}_{norm}(\mathbf{r})$ both fluctuate [see Eq. (4)]. In the following, we turn to the main topic of this paper, namely, the analysis of the distribution of local electric field strengths $|\mathbf{E}_{norm}(\mathbf{r})|$ in matrix and particles. First, we shall vary the dielectric ratio for given filling factors, and then we keep the dielectric ratio constant and vary the filling factor.

A. Variation of dielectric ratio

In Figs. 9(a) and 9(b), we display the distributions of local electric field strengths $|\mathbf{E}_{norm}(\mathbf{r})|$ in the particles and matrix, respectively, as well as the corresponding average values (vertical lines) for three composites with a particle volume fraction of $f = 0.1$. The dielectric ratio was varied, resulting in different effective permittivities (determined via the simulated S-parameters; see Sec. III): $\varepsilon_{eff}/\varepsilon_m = 1.079$ for $\varepsilon_p/\varepsilon_m = 2$, $\varepsilon_{eff}/\varepsilon_m = 1.183$ for $\varepsilon_p/\varepsilon_m = 5$, and $\varepsilon_{eff}/\varepsilon_m = 1.228$ for $\varepsilon_p/\varepsilon_m = 8$.

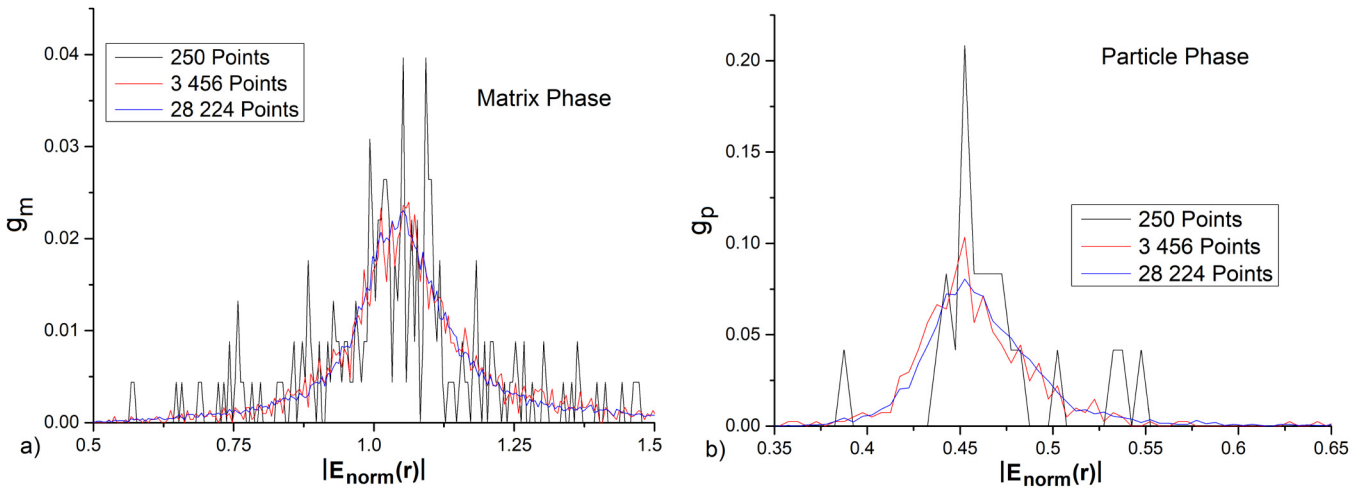

FIG. 7. Distributions of $|\mathbf{E}_{norm}(\mathbf{r})|$ in matrix (a) and particles (b) for different numbers of field amplitudes, N_{points}. Parameters were chosen as $\varepsilon_p/\varepsilon_m = 5$, $N_{inc} = 200$ ($r = 0.068$ cm), $f = 0.1$, and three mesh refinement passes.

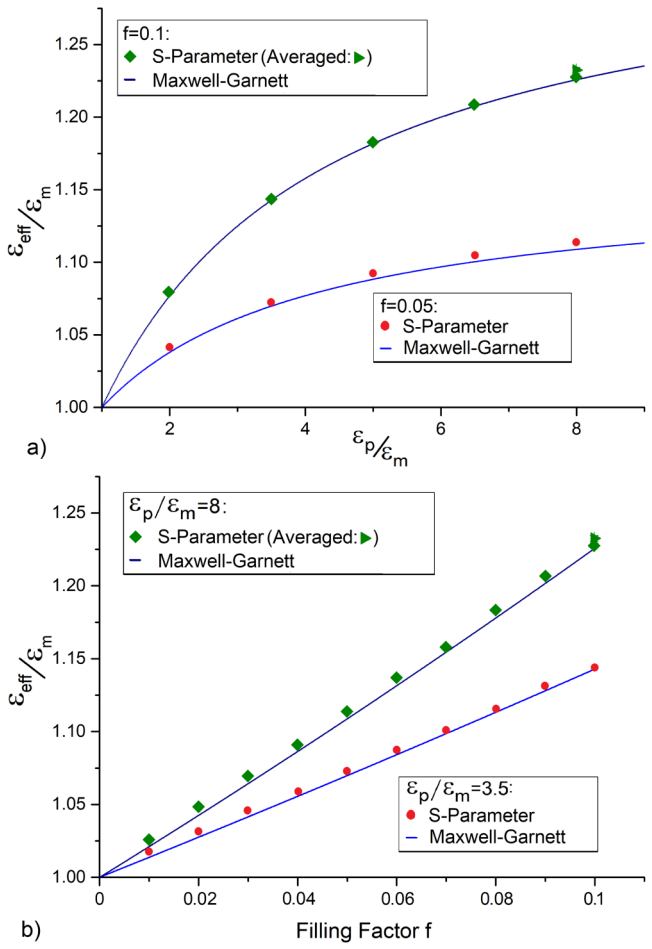

FIG. 8. Ratio of effective permittivity to matrix permittivity for composites as a function of the dielectric ratio (a) and of the filling factor (b). The analytical solution for a random dispersion of monodisperse spheres, i.e., the Maxwell–Garnett formula (21) (curves), is compared with simulated data (symbols), i.e., with $\varepsilon_{\text{eff}}/\varepsilon_m$ values obtained via the *S*-parameters (see Sec. III). The simulated $\varepsilon_{\text{eff}}/\varepsilon_m$ data exhibit a maximum deviation of 0.5% at $\varepsilon_p/\varepsilon_m = 8$ and $f = 0.1$. For the latter parameters, we display both the result of a single simulation run and the average value for ten different particle configurations.

While the peaks in the particle phase clearly shift toward weaker fields with increasing $\varepsilon_p/\varepsilon_m$ [see Fig. 9(a)], they move slightly toward higher fields in the matrix phase [see Fig. 9(b)]. The dependence on the dielectric ratio is displayed in Figs. 9(c) and 9(d). The curves are the analytical solutions for the average field amplitudes $\langle E_{\text{norm},y}(\mathbf{r})\rangle_p$ and $\langle E_{\text{norm},y}(\mathbf{r})\rangle_m$, respectively, calculated from Eqs. (11) and (12) using ε_{eff} values according to the Maxwell–Garnett formula (21) [remember that these values are correlated according to Eq. (10)]. They are in good agreement with those calculated by inserting the simulated effective permittivities into Eqs. (11) and (12) (green symbols). We also show the average values of the field strength $\langle|\mathbf{E}_{\text{norm}}(\mathbf{r})|\rangle_p$ and $\langle|\mathbf{E}_{\text{norm}}(\mathbf{r})|\rangle_m$ obtained from an analysis of the simulated distributions of electric field strengths [see Eqs. (18) and 19]. These are slightly higher than the values specified above, in agreement with what we can expect: $\langle|\mathbf{E}_{\text{norm}}(\mathbf{r})|\rangle_i \geq |\langle\mathbf{E}_{\text{norm}}(\mathbf{r})\rangle_i| = \langle E_{\text{norm},y}(\mathbf{r})\rangle_i$ holds for both constituents ($i = p, m$).[48] For example, at $\varepsilon_p/\varepsilon_m = 8$ and $f = 0.1$, our simulations yield a value for $\langle|\mathbf{E}_{\text{norm}}(\mathbf{r})|\rangle_p$ that is about 10% higher than the value for $\langle E_{\text{norm},y}(\mathbf{r})\rangle_p$, while the value for $\langle|\mathbf{E}_{\text{norm}}(\mathbf{r})|\rangle_m$ is about 2.3% higher than the value for $\langle E_{\text{norm},y}(\mathbf{r})\rangle_m$. Apart from these small differences, the average values of both distributions, i.e., of $|\mathbf{E}_{\text{norm}}(\mathbf{r})|$ and of $E_{\text{norm},y}(\mathbf{r})$, follow the same trend: the higher the dielectric ratio, the lower is the average field strength in the particles and the higher is the average field strength in the matrix. For $\varepsilon_p/\varepsilon_m > 1$, the average normalized field strength in the particles is smaller than 1, while it is larger than 1 in the matrix. In other words, compared with a homogeneous material of permittivity ε_{eff}, the particles exhibit on average a lower field strength, while the matrix exhibits on average a higher one.

To elucidate the above behavior, we consider a simplified situation where a single dielectric sphere of permittivity $\varepsilon_p > 1$ in vacuum is exposed to a uniform external field $\mathbf{E}_0$. The material is polarized, and so, the resulting surface charges give rise to a depolarization field inside the sphere and a dipolar field outside it. The depolarization field weakens the applied field, i.e., the field $\mathbf{E}_{\text{in}}$ inside the sphere is reduced,[49]

$$\mathbf{E}_{\text{in}} = \frac{3}{\varepsilon_p + 2}\mathbf{E}_0, \tag{22}$$

while the dipolar field outside the sphere enhances the field strength in its vicinity.

Next, we analyze the width of the distributions. For this purpose, we evaluate the standard deviations σ_p and σ_m of the distributions of the local field strengths $|\mathbf{E}_{\text{norm}}(\mathbf{r})|$ in the particles and in the matrix. The variance σ_i^2 is the mean of all squared deviations from $\langle|\mathbf{E}_{\text{norm}}|\rangle_i$, and so

$$\sigma_i = \sqrt{\langle(|\mathbf{E}_{\text{norm}}|_i - \langle|\mathbf{E}_{\text{norm}}|\rangle_i)^2\rangle} \qquad (i = p, m) \tag{23}$$

holds. An alternative way to present the data would be to normalize the standard deviations with respect to the mean values in the particular phase,[12,13] dividing the above expression by $\langle|\mathbf{E}_{\text{norm}}|\rangle_i$. We make use of Eq. (23), allowing us a direct comparison of the field distributions on the same scale.

The result is displayed in Figs. 9(e) and 9(f). Obviously, the distributions in both phases broaden with increasing dielectric ratio, and the values for σ_p and σ_m are quite similar. Thus, at high dielectric contrast, $\sigma_p/\langle|\mathbf{E}_{\text{norm}}|\rangle_p$ becomes many times higher than $\sigma_m/\langle|\mathbf{E}_{\text{norm}}|\rangle_m$. As already mentioned in Sec. IV, the number of particles in our simulations is limited to $N_{\text{inc}} = 200$, and so especially the distributions of local field strengths in the particle phase can be noisy at high dielectric contrast (cf. Fig. 5). To check whether this statistical error has any influence on the standard deviations that we evaluate, we simulated ten different microstructures with $f = 0.1$ and $\varepsilon_p/\varepsilon_m = 8$. The average mean values of σ_p and σ_m as well as the corresponding fluctuations (standard deviations of the mean values) are also shown in Figs. 9(e) and 9(f). As

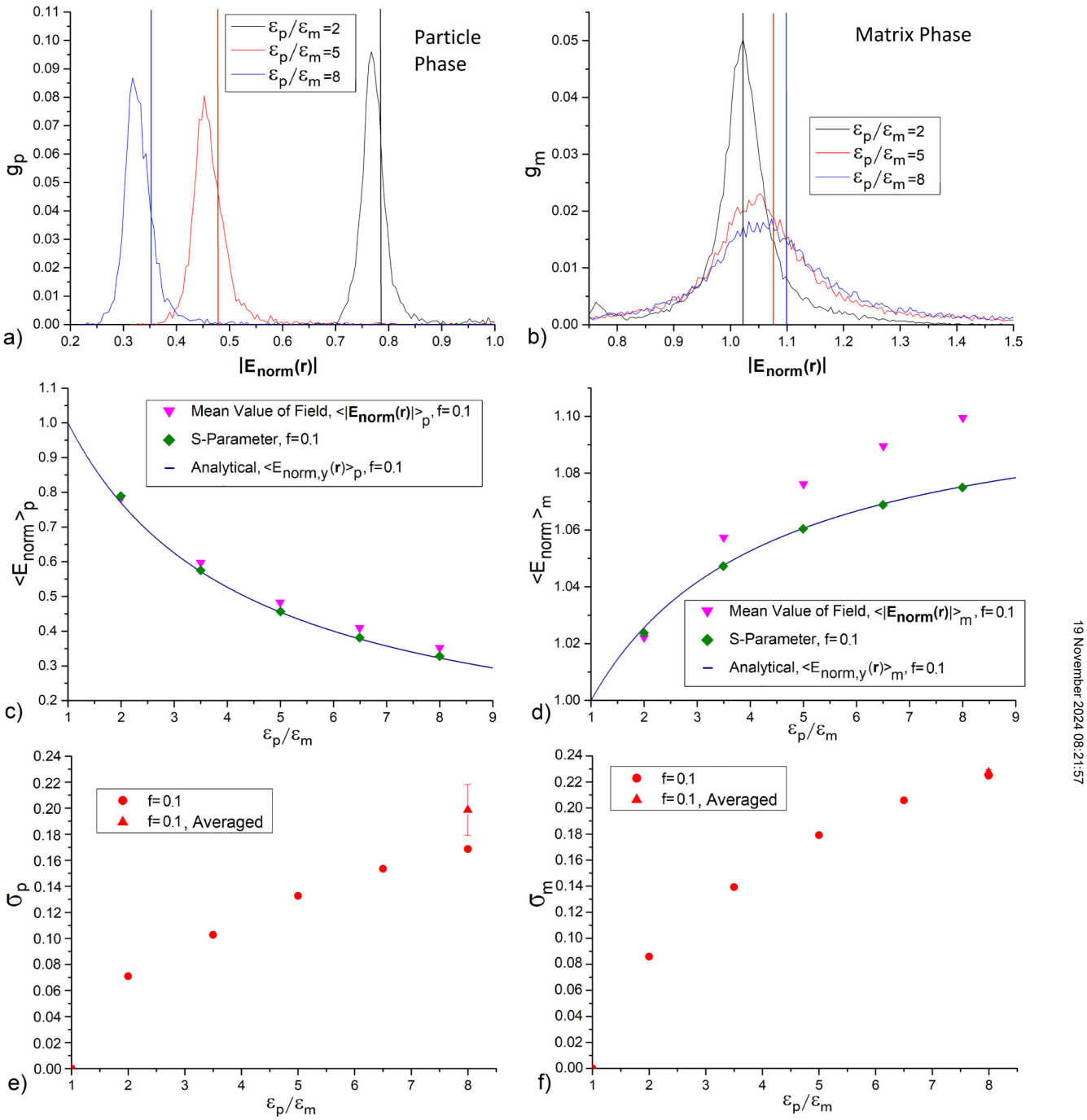

FIG. 9. (a) and (b) Simulated distributions of $|\mathbf{E}_{norm}(\mathbf{r})|$ in particles (left) and matrix (right) of composites with filling factor $f = 0.1$ but different dielectric ratios $\varepsilon_p/\varepsilon_m = 2$ (black), 5 (red), and 8 (blue). The vertical lines indicate the respective mean values. (c) and (d) Values of average field amplitudes $\langle E_{norm,y}(\mathbf{r})\rangle_p$ and $\langle E_{norm,y}(\mathbf{r})\rangle_m$ in particles (left) and matrix (right) vs dielectric ratio calculated from Eqs. (11) and (12): the curves are the analytical solution using ε_{eff} values according to the Maxwell–Garnett formula (21), while the green diamonds correspond to values calculated using simulated effective permittivities. As expected, the average values of the field strengths $\langle|\mathbf{E}_{norm}(\mathbf{r})|\rangle_p$ and $\langle|\mathbf{E}_{norm}(\mathbf{r})|\rangle_m$ (purple triangles) are higher. These are obtained by analyzing the simulated distributions [see (a) and (b)]. (e) and (f) Standard deviations σ_p and σ_m in particles and matrix (red spheres) characterizing the width of the distributions of $|\mathbf{E}_{norm}(\mathbf{r})|$. At $\varepsilon_p/\varepsilon_m = 8$, we also display the mean values obtained by averaging the results of ten different random particle configurations as well as the corresponding standard deviations (red triangles with error bars).

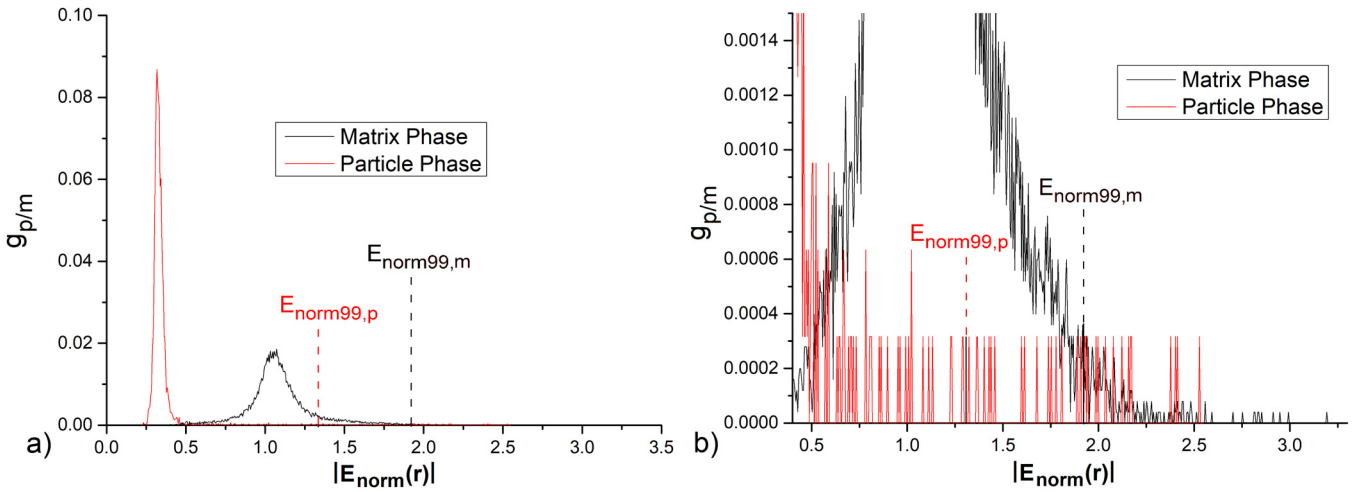

FIG. 10. (a) Distributions g_p and g_m of local field strengths in both the particle (red) and matrix (black) phases of a composite with $\varepsilon_p/\varepsilon_m = 8$ and $f = 0.1$. (b) Enlargement at high field strengths.

expected, statistical fluctuations are much higher in the particles than in the matrix.

A closer look at Figs. 9(a) and 9(b) reveals that the distributions of local field strengths become asymmetric, with a preference for higher field strengths, when $\varepsilon_p/\varepsilon_m$ increases. For this reason, the respective mean values are located at the right side of the most frequent field strength (the maximum of the distribution). In Fig. 10, we display the distributions of $|\mathbf{E}_{norm}(\mathbf{r})|$ in particles and matrix for a composite with $f = 0.1$ and $\varepsilon_p/\varepsilon_m = 8$. Zooming in reveals the contributions at high field strengths, i.e., far above the respective average values. To quantify this observation, we calculate the first (E_{norm1}) and 99th (E_{norm99}) percentiles of the distributions, i.e., the field strengths separating the lowest and highest percent of the distribution (see the vertical dashed lines in Fig. 10): 1% of the $|\mathbf{E}_{norm}(\mathbf{r})|$ values in the particles are higher than $E_{norm99,p}$ and 1% are lower than $E_{norm1,p}$. Analogous definitions hold for the matrix. The results are shown in Fig. 11. For both the particles and the matrix, E_{norm99} increases with increasing dielectric ratio, while

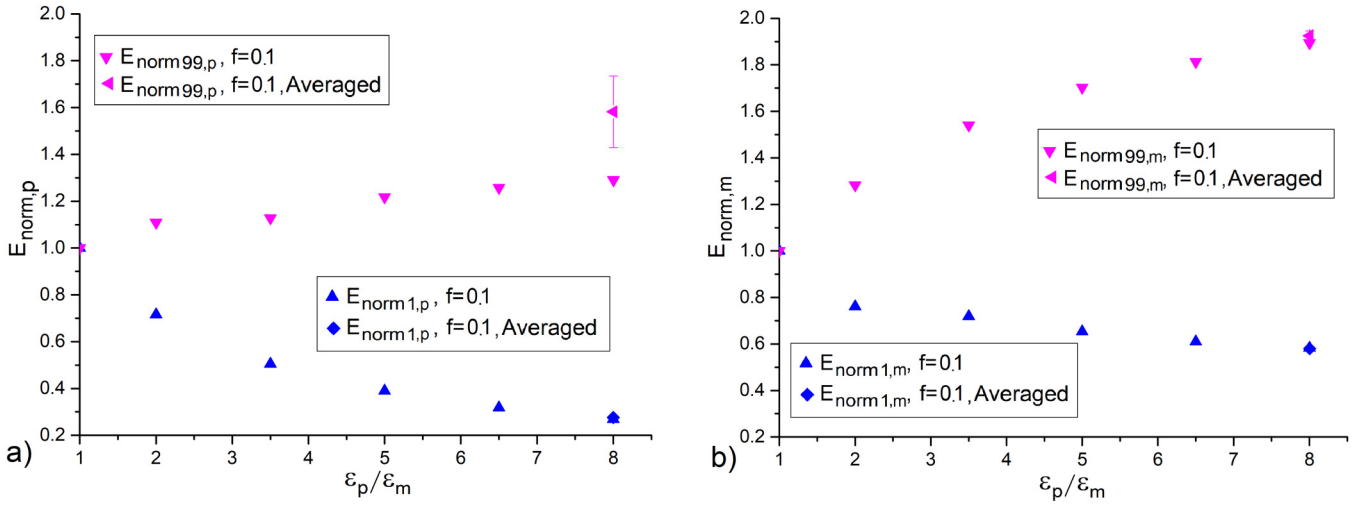

FIG. 11. Field strengths corresponding to the highest and lowest percentiles of the distributions of $|\mathbf{E}_{norm}(\mathbf{r})|$ in particles (a) and matrix (b) vs dielectric contrast. At $\varepsilon_p/\varepsilon_m = 8$, we also display the mean values obtained by averaging the results of ten different random particle configurations as well as the corresponding standard deviations (symbols with error bars).

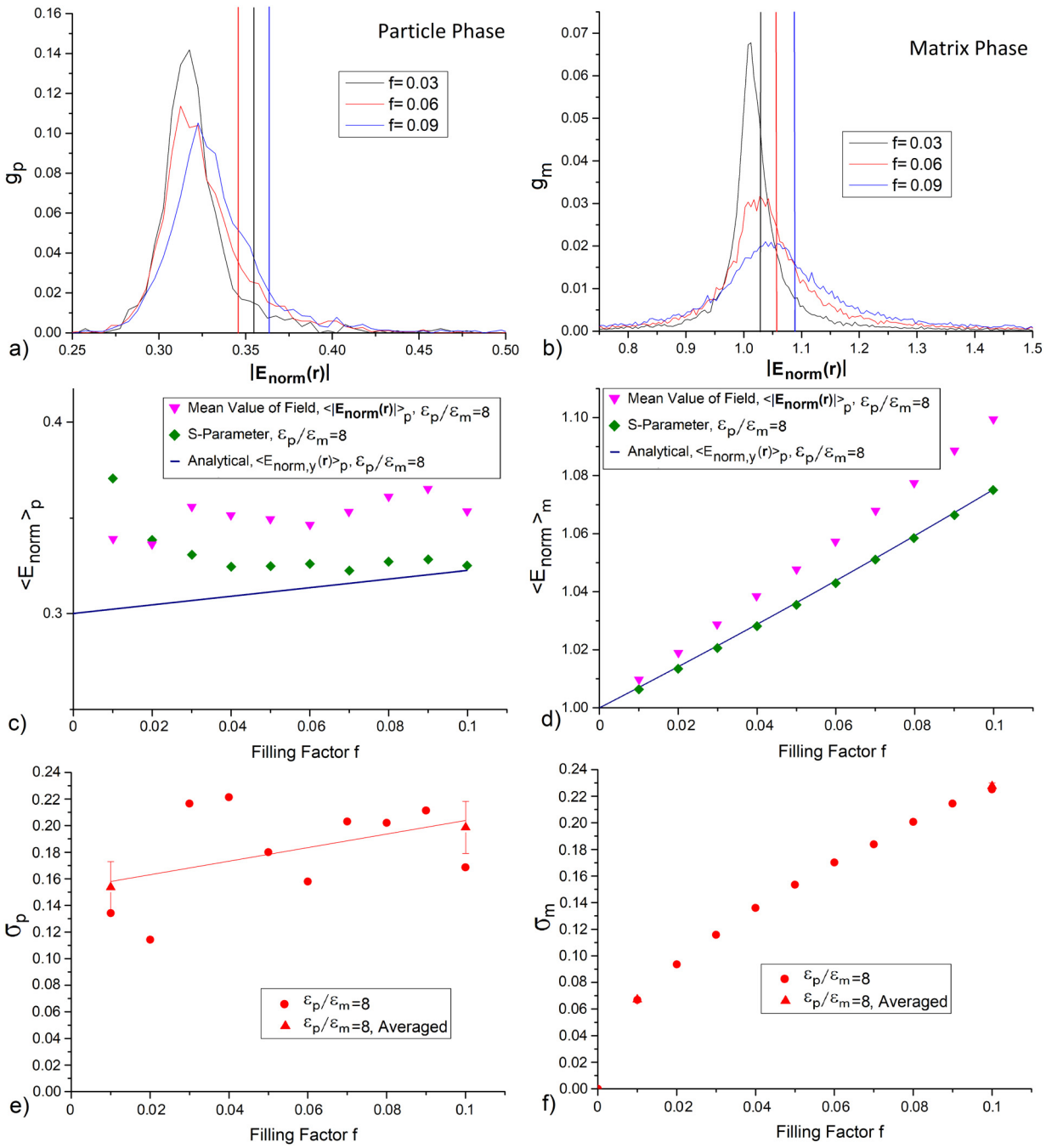

FIG. 12. (a) and (b) Simulated distributions of local field strengths $|\mathbf{E}_{norm}(\mathbf{r})|$ in particles and matrix, respectively, of composites with a dielectric ratio $\varepsilon_p/\varepsilon_m = 8$ but different volume filling factors $f = 0.03$ (black), 0.06 (red), and 0.09 (blue). The vertical lines indicate the respective mean values. (c) and (d) Values of the average field amplitudes $\langle E_{norm,y}(\mathbf{r})\rangle_p$ and $\langle E_{norm,y}(\mathbf{r})\rangle_m$ in particles and matrix, respectively, vs the volume filling factor, calculated from Eqs. (11) and (12). The curves are the analytical solution using ε_{eff} values according to the Maxwell–Garnett formula (21), while the green diamonds correspond to values calculated using simulated effective permittivities. As expected, the average values of the field strength $\langle|\mathbf{E}_{norm}(\mathbf{r})|\rangle_p$ and $\langle|\mathbf{E}_{norm}(\mathbf{r})|\rangle_m$ (purple triangles) are higher. These are obtained by analyzing the simulated distributions [see (a) and (b)]. (e) and (f) Standard deviations σ_p and σ_m characterizing the widths of the $|\mathbf{E}_{norm}(\mathbf{r})|$ distributions in particles and matrix, respectively. At $f = 0.01$ and $f = 0.1$, we also display the mean values obtained by averaging the results of ten different random particle configurations as well as the corresponding standard deviations (red triangles with error bars). The straight line in (e) is a linear fit of the simulated data.

E_{norm1} decreases. This behavior reflects the broadening of the distributions. The arithmetical mean of $E_{\mathrm{norm1},m}$ and $E_{\mathrm{norm99},m}$ is rather close to the average value $\langle|\mathbf{E}_{\mathrm{norm}}(\mathbf{r})|\rangle_m$ [cf. Figs. 9(d) and 11(b)]. In contrast, the distributions in the particles [see Fig. 9(a)] are more asymmetric, i.e., both the average value $\langle|\mathbf{E}_{\mathrm{norm}}(\mathbf{r})|\rangle_p$ and $E_{\mathrm{norm1},p}$ decrease with increasing dielectric ratio, while $E_{\mathrm{norm99},p}$ increases [cf. Figs. 9(c) and 11(a)]. To illustrate the enhancement of the local electric field strength in some domains of the sample, we choose as an example a dielectric ratio $\varepsilon_p/\varepsilon_m = 8$ at a filling factor of $f = 0.1$. The highest percentile of field strengths in the particles exhibits values that are more than 1.6 times higher than the field strength in a homogeneous material of permittivity $\varepsilon_{\mathrm{eff}}$. For the matrix, even $E_{\mathrm{norm99},m} \simeq 1.9$ holds. Nevertheless, compared with the respective average field strengths in particles and matrix [cf. Figs. 9(c) and 9(d)], the relative change is much stronger in the particles. We obtain $E_{\mathrm{norm99},p}/\langle|\mathbf{E}_{\mathrm{norm}}(\mathbf{r})|\rangle_p \simeq 1.6/0.356 \simeq 4.5$, compared with $E_{\mathrm{norm99},m}/\langle|\mathbf{E}_{\mathrm{norm}}(\mathbf{r})|\rangle_m \simeq 1.9/1.1 \simeq 1.7$.

B. Variation of filling factor

As in Sec. V A, we start with three examples of composites [see Figs. 12(a) and 12(b)], i.e., we display the distributions of local field strengths $|\mathbf{E}_{\mathrm{norm}}(\mathbf{r})|$ in inclusions and matrix, respectively, as well as the corresponding average values (vertical lines). But now the dielectric ratio $\varepsilon_p/\varepsilon_m = 8$ is kept constant while the particle concentration is varied. To realize different volume fractions of particles while preserving their number $N_{\mathrm{inc}} = 200$ as well as the geometric dimensions of the samples, we have adapted the particle radii according to Eq. (20). Evaluating the S parameters of the simulations (see Sec. III), we obtain the following effective permittivities: $\varepsilon_{\mathrm{eff}}/\varepsilon_m = 1.069$ for $f = 0.03$ ($r = 0.046$ cm), $\varepsilon_{\mathrm{eff}}/\varepsilon_m = 1.137$ for $f = 0.06$ ($r = 0.058$ cm), and $\varepsilon_{\mathrm{eff}}/\varepsilon_m = 1.207$ for $f = 0.09$ ($r = 0.066$ cm).

With increasing f, the average field strength in the matrix phase, $\langle|\mathbf{E}_{\mathrm{norm}}(\mathbf{r})|\rangle_m$, shifts toward higher field strengths, while no clear trend is observed in the particle phase, i.e., for $\langle|\mathbf{E}_{\mathrm{norm}}(\mathbf{r})|\rangle_p$ [see the vertical lines in Figs. 12(a) and 12(b)]. All these values lie above the most frequent field strength (position of the peak), reflecting an asymmetric broadening of the distributions, especially in the particle phase.

In Figs. 12(c) and 12(d), we display the dependence of the various mean field amplitudes and field strengths on the filling factor. As in Sec. V A [cf. Figs. 9(c) and 9(d)], the curves correspond to the analytical solutions for the field amplitudes $\langle E_{\mathrm{norm},y}(\mathbf{r})\rangle_p$ and $\langle E_{\mathrm{norm},y}(\mathbf{r})\rangle_m$ calculated from Eqs. (11) and (12) using $\varepsilon_{\mathrm{eff}}$ values according to the Maxwell–Garnett formula (21). Compared with a homogeneous material of permittivity $\varepsilon_{\mathrm{eff}}$, the particles exhibit on average a lower field amplitude, $\langle E_{\mathrm{norm},y}(\mathbf{r})\rangle_p < 1$, while the matrix exhibits on average a higher one, $\langle E_{\mathrm{norm},y}(\mathbf{r})\rangle_m > 1$. But both mean values increase linearly by 7.5% when the filling factor is enhanced to $f = 0.1$. As before, the shift can be explained phenomenologically by the accumulation of charges on the surfaces of the particles. These enforce the electric fields outside the particles on which they are located and thereby create an environment of higher field values for all surrounding particles. Of course, the influence of this effect grows as more dielectric material is included. Consequently, both particles and matrix are affected by higher electric fields. There is good agreement with the values calculated inserting the simulated effective permittivities (obtained via the S-parameters) in Eqs. (11) and (12) (green symbols), at least for the matrix phase. However, for the particle phase, the numerical error increases in the limit $f \to 0$ [then $\varepsilon_{\mathrm{eff}}/\varepsilon_m$ approaches one, but small deviations in the

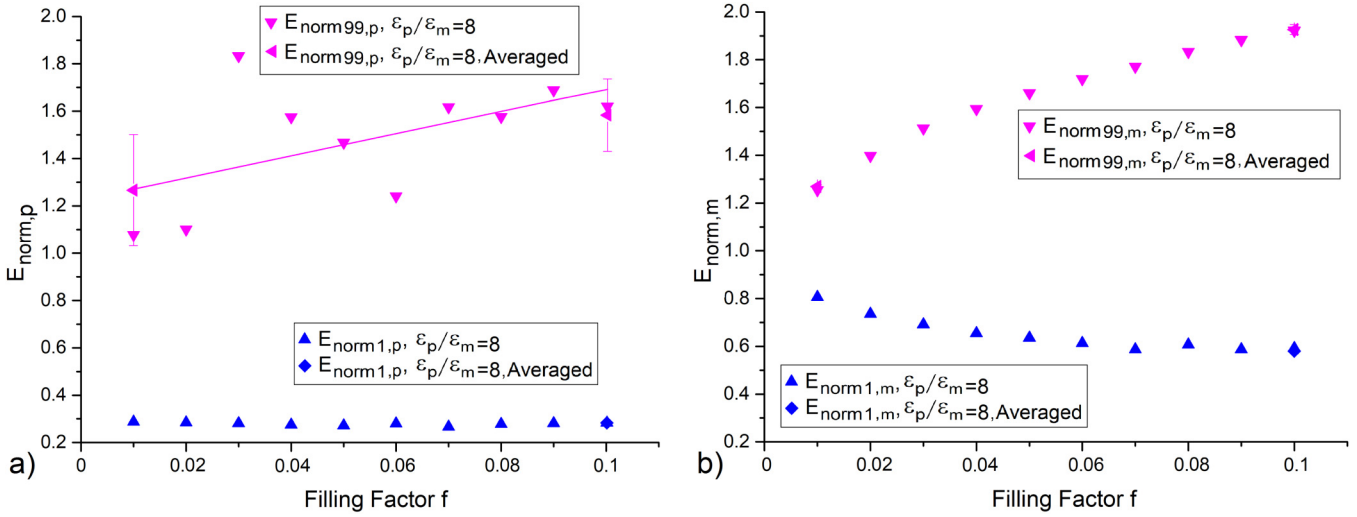

FIG. 13. Field strengths corresponding to the highest and lowest percentiles of the distributions of local field strengths $|\mathbf{E}_{\mathrm{norm}}(\mathbf{r})|$ in particles (a) and matrix (b) vs volume filling factor. At $f = 0.01$ and $f = 0.1$, we also display the mean values obtained by averaging the results of ten different random particle configurations as well as the corresponding standard deviations (symbols with error bars). The straight line in (a) is a linear fit of the simulated data.

S-parameters induce errors in $\varepsilon_{\mathrm{eff}}/\varepsilon_m$ and, thus, in $\langle E_{\mathrm{norm},y}(\mathbf{r})\rangle_p$; see Eq. (11)]. We also show the average field strengths $\langle|\mathbf{E}_{\mathrm{norm}}(\mathbf{r})|\rangle_p$ and $\langle|\mathbf{E}_{\mathrm{norm}}(\mathbf{r})|\rangle_m$ obtained from an analysis of the simulated field distributions [see Eqs. (18) and (19)]. As expected, these are slightly higher than the values for the amplitudes specified above.

Next, we turn to the widths of the distributions of $|\mathbf{E}_{\mathrm{norm}}(\mathbf{r})|$ in the particles and in the matrix, i.e., to the standard deviations σ_p and σ_m [see Figs. 12(e) and 12(f)]. In the particle phase, the σ_p values suffer from strong perturbations, and so the plot does not reveal a clear dependence on particle concentration (remember that the number of particles in our simulations is limited to $N_{\mathrm{inc}} = 200$, and therefore, the distributions, especially in the particle phase, can be noisy; cf. Fig. 5). But a linear fit seems to indicate a weak growth of σ_p with increasing volume filling factor. This observation is confirmed by averaging the data for ten different microstructures at $f = 0.01$ and $f = 0.1$ (the error bars indicate the standard deviation of the corresponding mean values). With regard to the matrix phase, the standard deviation σ_m increases markedly with increasing filling factor, similar to what we have observed for increasing dielectric ratio [cf. Fig. 9(f)].

Finally, we analyze field strengths below and above the average value, i.e., those separating the lowest and highest percentiles of a distribution, E_{norm1} and E_{norm99}. The results are shown in Fig. 13. In the particle phase, the values of $E_{\mathrm{norm1},p}$ are almost independent

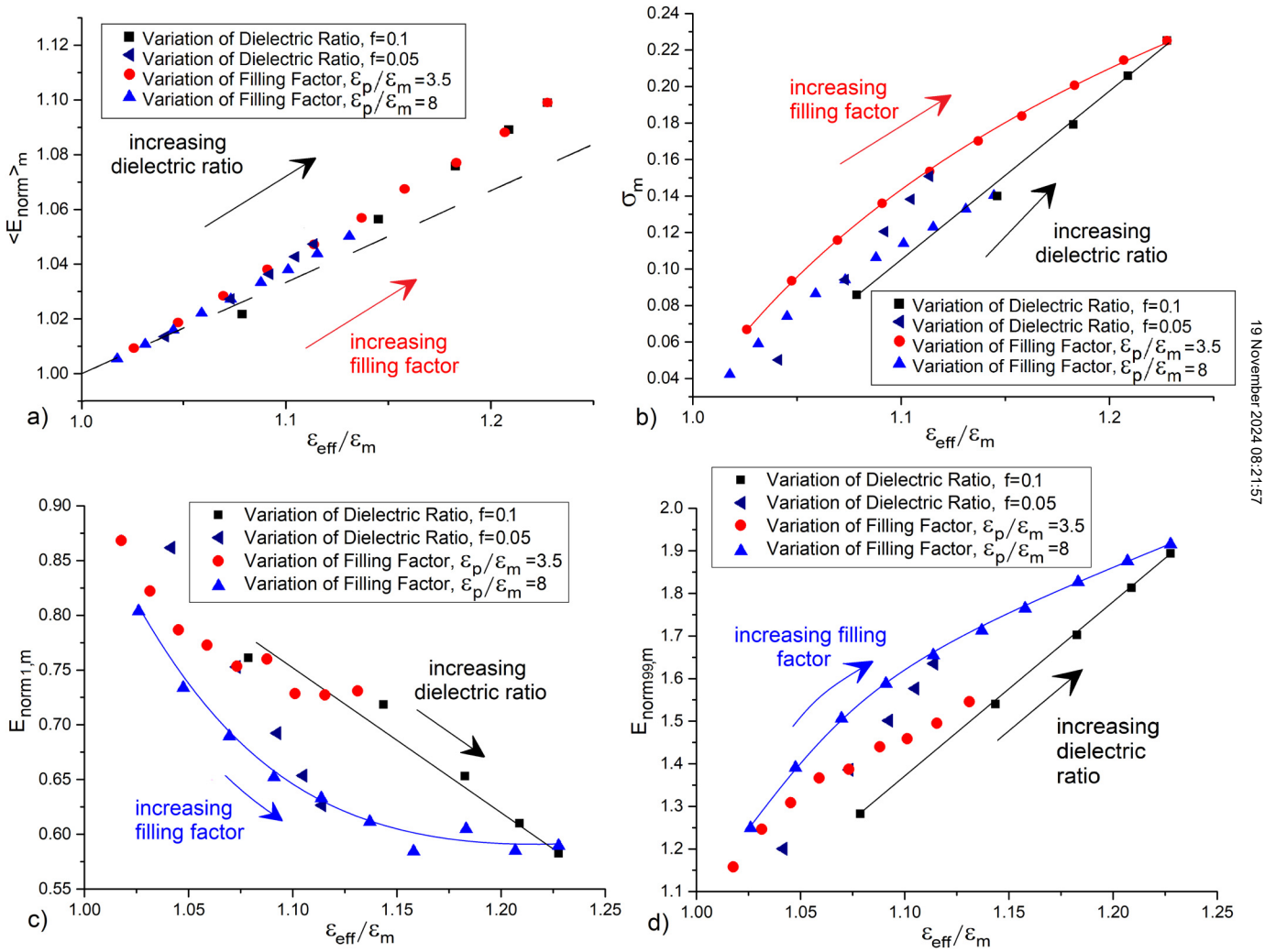

FIG. 14. Characteristic properties of the field distribution in the matrix phase as a function of the normalized effective permittivity $\varepsilon_{\mathrm{eff}}/\varepsilon_m$ for composites with filling factors ranging from $f = 0.01$ to 0.1 and dielectric ratios from $\varepsilon_p = 2$ to 8. (a) Mean field strength $\langle|\mathbf{E}_{\mathrm{norm}}(\mathbf{r})|\rangle_m$. The dashed line represents the lower bound given by Eq. (24). (b) Standard deviation σ_m. (c) and (d) Field strengths corresponding to the lowest and highest percentiles, respectively, of the distributions of local electric field strengths $|\mathbf{E}_{\mathrm{norm}}(\mathbf{r})|$. The curves in (b)–(d) are guides for the eye.

of the filling factor and rather close to the average values $\langle|\mathbf{E}_{\mathrm{norm}}(\mathbf{r})|\rangle_p$ [cf. Fig. 12(c)]. In contrast, $E_{\mathrm{norm99},p}$ shows a perturbed but slightly growing behavior. Considering the matrix phase, we obtain growing values for $E_{\mathrm{norm99},m}$ characterizing the highest percentile and decreasing values for $E_{\mathrm{norm1},m}$ characterizing the lowest percentile, and their arithmetical mean is rather close to the average value $\langle|\mathbf{E}_{\mathrm{norm}}(\mathbf{r})|\rangle_m$ [cf. Figs. 13(b) and 12(d)]. For both phases, higher volume fractions of inclusions lead to a spreading of the difference between E_{norm1} and E_{norm99}, in accordance with the previously discussed broadening of the distributions.

C. Identification of common features

In Secs. V A and V B, we have shown how the distributions of local electric field strengths change when the dielectric ratio $\varepsilon_p/\varepsilon_m$ or the volume filling factor f of the particles is increased. Since

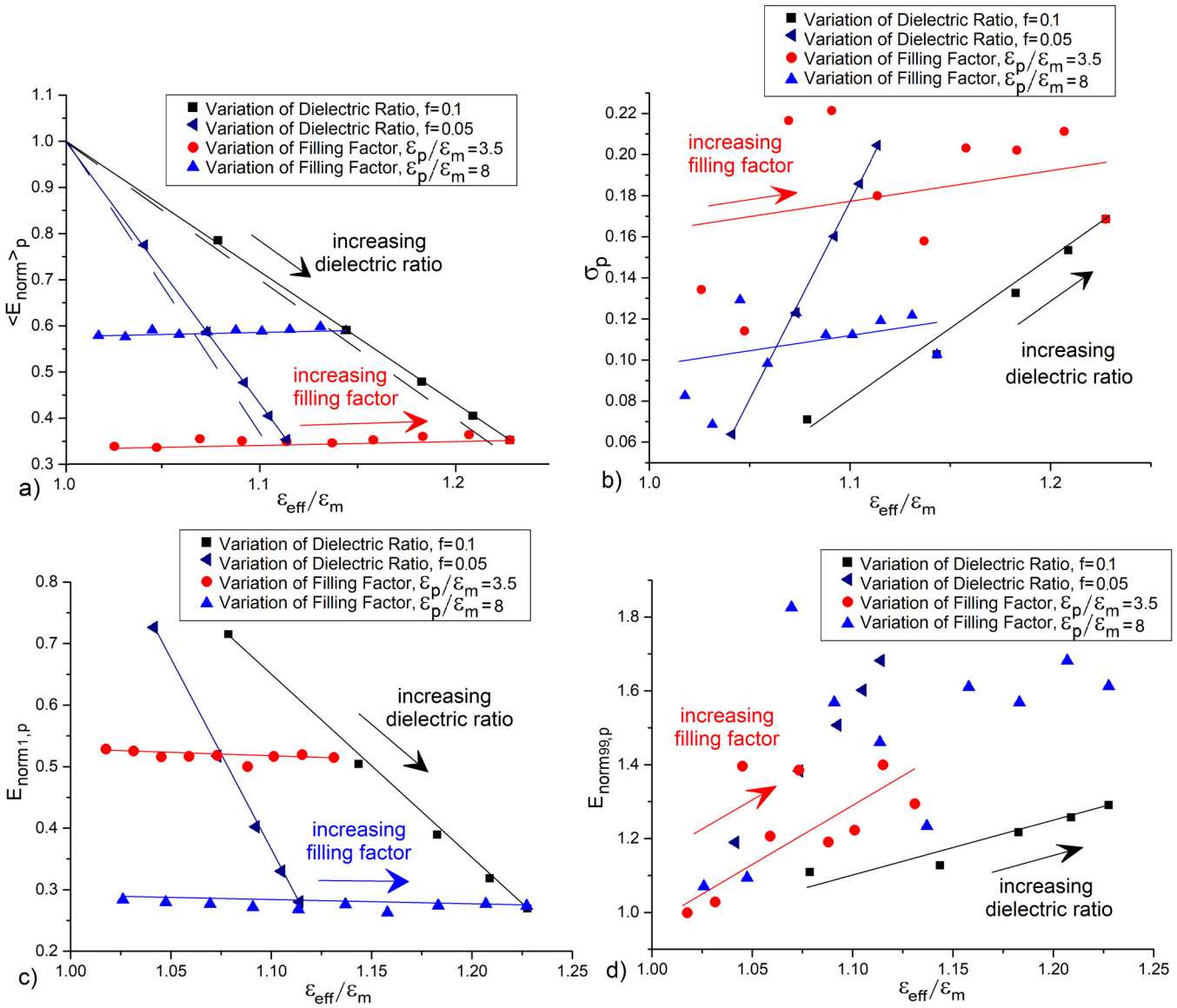

FIG. 15. Characteristic properties of the distribution of local electric field strengths in the particles as a function of the normalized effective permittivity $\varepsilon_{\mathrm{eff}}/\varepsilon_m$ for composites with filling factors ranging from $f = 0.01$ to 0.1 and dielectric ratios from $\varepsilon_p = 2$ to 8. The solid lines are guides for the eye. (a) Mean field strength $\langle|\mathbf{E}_{\mathrm{norm}}(\mathbf{r})|\rangle_p$. The dashed lines represent the lower bound given by Eq. (25) for $f = \mathrm{const}$. (b) Standard deviation σ_p. (c) and (d) Field strengths corresponding to the lowest and highest percentiles, respectively, of the distribution of $|\mathbf{E}_{\mathrm{norm}}(\mathbf{r})|$.

both variations go along with an increase in the normalized effective permittivity $\varepsilon_{\text{eff}}/\varepsilon_m$ (see Fig. 8), we can recapitulate our results, condensing the data in common diagrams (and adding data from simulation runs not shown previously).

With regard to the matrix, increases in the dielectric ratio $\varepsilon_p/\varepsilon_m$ and in the volume filling factor f have similar impacts on the characteristics of the distribution (see Fig. 14). The mean field strength $\langle|\mathbf{E}_{\text{norm}}(\mathbf{r})|\rangle_m$ increases linearly as a function of $\varepsilon_{\text{eff}}/\varepsilon_m$ [see Fig. 14(a)]. This behavior is characteristic of a composite with a random spatial distribution of monodisperse spheres, where the effective permittivity is given by the Maxwell–Garnett formula (21). Solving this equation for $\varepsilon_p/\varepsilon_m$ and inserting the result into Eq. (12) yield

$$\langle E_{\text{norm},y}\rangle_m = 1 + \frac{1}{3}\left(\frac{\varepsilon_{\text{eff}}}{\varepsilon_m} - 1\right) \tag{24}$$

for the field amplitude. Since $\langle|\mathbf{E}_{\text{norm}}(\mathbf{r})|\rangle_m \geq \langle E_{\text{norm},y}\rangle_m$ holds, the above equation is a lower bound on the simulated values of the field strength displayed in Fig. 14(a). In fact, these lie on a straight line, the slope of which is higher than the value of 1/3 predicted for $\langle E_{\text{norm},y}\rangle_m$. The inequality $\langle|\mathbf{E}_{\text{norm}}(\mathbf{r})|\rangle_m \geq 1$ holds, i.e., compared with a homogeneous material of permittivity ε_{eff}, the matrix material is on average exposed to a slightly higher field strength [up to 10% for the data displayed in Fig. 14(a)]. The higher the effective permittivity, the broader is the distribution: the standard deviation σ_m as well as the field strength $E_{\text{norm99},m}$ of the highest percentile increase [note the similar dependences on $\varepsilon_{\text{eff}}/\varepsilon_m$ in Figs. 14(b) and 14(d)], while the field strength $E_{\text{norm1},m}$ of the lowest percentile decreases [Fig. 14(c)]. For the range of data displayed, we obtain values up to $E_{\text{norm99},m} \simeq 1.9$, i.e., a field strength about twice that in a homogeneous material of permittivity ε_{eff}.

The characteristics of the distribution of local electric field strengths in the particles are shown in Fig. 15. For the mean field strength in the particles, $\langle|\mathbf{E}_{\text{norm}}(\mathbf{r})|\rangle_p \leq 1$ holds [see Fig. 15(a)], i.e., the particles exhibit on average a field strength that is lower than that of a homogeneous material of permittivity ε_{eff} by a factor $1/\langle|\mathbf{E}_{\text{norm}}(\mathbf{r})|\rangle_p \simeq 1.3{-}2.9$ for the data shown ($\varepsilon_p/\varepsilon_m \in [2, 8]$ and $f \in [0, 0.1]$). The higher the dielectric ratio of the constituents, $\varepsilon_p/\varepsilon_m$, the lower is the mean field strength in the particles. Inserting Eq. (24) into Eq. (10) yields for the field amplitude,

$$\langle E_{\text{norm},y}\rangle_p = 1 - \frac{1-f}{3f}\left(\frac{\varepsilon_{\text{eff}}}{\varepsilon_m} - 1\right), \tag{25}$$

in accordance with the linear decrease in $\langle|\mathbf{E}_{\text{norm}}(\mathbf{r})|\rangle_p \geq \langle E_{\text{norm},y}\rangle_p$ with increasing $\varepsilon_{\text{eff}}/\varepsilon_m$ observed in Fig. 15(a) for constant f and increasing $\varepsilon_p/\varepsilon_m$. For a constant dielectric ratio, the increases in f and $\varepsilon_{\text{eff}}/\varepsilon_m$ nearly compensate, and so the field amplitude $\langle E_{\text{norm},y}\rangle_p$ increases only slightly and the field strength $\langle|\mathbf{E}_{\text{norm}}(\mathbf{r})|\rangle_p$ is nearly constant [cf. Figs. 12(c) (curve) and 15(a)]. Analogously, an increase of $\varepsilon_p/\varepsilon_m$ results in a marked enhancement of the standard deviation σ_p, i.e., in a strong broadening of the distribution of local field strengths, while the effect of a variation in f is hardly noticeable [see Fig. 15(b)]. The field strength $E_{\text{norm1},p}$ of the lowest percentile follows the trends observed for the mean value

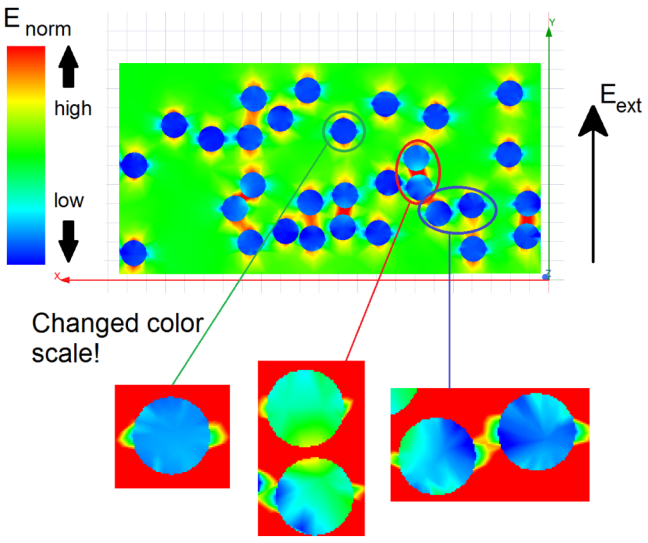

FIG. 16. The color map at the top shows the spatial distribution of electric field strengths in a composite consisting of 30 dielectric spheres located in one plane and exposed to an applied electric field in the y direction. The range of electric field strengths is coded from blue (low) to green (average) to red (high). The enlarged sections at the bottom show (from left to right) spatial field distributions for an isolated sphere, a parallel orientated pair of spheres, and a perpendicular agglomeration of two inclusions. Note that the color range in these sections has been changed to highlight field fluctuations in the matrix and in the particles: areas of low field strength are still colored blue, but now areas of average field strength are colored red.

$\langle|\mathbf{E}_{\text{norm}}(\mathbf{r})|\rangle_m$ [cf. Figs. 15(a) and 15(c)]: it decreases when the dielectric ratio is increased but remains approximately constant when only the filling factor is varied. The field strength $E_{\text{norm99},p}$ of the highest percentile in the particle phase [Fig. 15(d)] increases when the dielectric ratio or the filling factor is enhanced. The data exhibit strong scatter, but we obtain values of $E_{\text{norm99},p}$ that are more than 1.6 times higher than the field strength in a homogeneous material of permittivity ε_{eff}. Compared with the average field strength in the particles [see Figs. 15(a) and 15(d)], the maximum relative change is even higher: $E_{\text{norm99},p}/\langle|\mathbf{E}_{\text{norm}}(\mathbf{r})|\rangle_p \simeq 1.6/0.356 \simeq 4.5$.

VI. SUMMARY AND CONCLUSIONS

The effective permittivity of a composite is related to the mean field amplitudes in its constituents, and, thus, the latter values can be determined either by experiment or by numerical simulations. However, in the majority of cases, the variations of the field values, i.e., width and form of the distribution, are only accessible via simulations. In this work, we have used numerical techniques to investigate the distribution of local electric field strengths in composites of dielectric spheres randomly dispersed in a homogeneous matrix ($\varepsilon_p/\varepsilon_m \geq 1$). We have assessed the accuracy of our results by reproducing analytical relations for the effective permittivity and the mean values of the normalized field amplitudes [see Eqs. (10)–(13)]. Our main results can be summarized as follows.

A composite of high effective permittivity can be obtained by increasing the particle concentration, the dielectric ratio of its constituents, or both. For the parameters chosen ($\varepsilon_p/\varepsilon_m \in [2, 8]$ and $f \in [0, 0.1]$), the average normalized field strength in the matrix remains close to 1, but the higher the dielectric ratio, the lower is the average field strength in the particles and the broader is the distribution. At the highest filling factor and dielectric ratio, the field strengths of the highest percentile in matrix and particles can reach values about twice the average field strength in the composite. In other words, in this case, 1% of the $|\mathbf{E}(\mathbf{r})|$ values in the composite are at least twice the field strength in a homogeneous material with the same permittivity ε_{eff}. As a consequence, local field strengths can exceed the mean values by far, even for random spatial distributions of particles.

Finally, we would like to give an idea of where such "high-field spots" are mainly located. We might visualize the electric field strength in a cross section of our 3D composites or even a plane of arbitrary orientation. But particles located outside such a 2D plane also influence the field distribution, and the resulting complex images are difficult to interpret. For ease of visualization and to highlight the essentials, we have generated an example of an "artificial" composite consisting of 30 monodisperse spheres, the centers of which are randomly dispersed in a 2D plane (more precisely in a cross section of the waveguide shown in Figs. 2 and 3). Once again, the electromagnetic fields have been calculated using a finite element solver as described in Sec. III. In Fig. 16, we display a color map of the spatial distribution of electric field strengths in the 2D plane, where the centers of the spheres are located. The lowest values of the field strength in the matrix occur between spheres that are perpendicularly orientated with respect to the external electric field (see the blue ellipse), while the highest values are found between spheres that are aligned parallel to the applied external field (see the red ellipse and compare with similar configurations: the closer the particles, the higher is the field strength). Analogously, high field strengths in the particles appear at the corresponding front surfaces of these configurations. Thus, even at a given filling factor f, the local interparticle spacing has an impact on the field strength. Here, we have generated our dielectric composites by sequential addition of hard spheres at random positions in the matrix, excluding overlap. Disordered systems with a higher portion of closely spaced particles can be generated by enhancing the probability that newly inserted particles are positioned in the vicinity of those inserted previously. Particle agglomeration might enforce the occurrence of "high-field spots", a conjecture that is to be checked and quantified by further simulations.

ACKNOWLEDGMENTS

We want to thank Cintia Hartmann and Charles Darwin Tchuimegni for carrying out preliminary studies in the framework of their master's theses as well as Béatrice Hallouet for helpful discussions.

AUTHOR DECLARATIONS

Conflict of Interest

The authors have no conflicts to disclose.

Author Contributions

Tobias Weber: Formal analysis (equal); Investigation (lead); Software (lead); Writing – original draft (equal). **Romanus Dyczij-Edlinger:** Resources (lead); Writing – original draft (supporting). **Rolf Pelster:** Conceptualization (lead); Formal analysis (equal); Writing – original draft (equal).

DATA AVAILABILITY

The data that support the findings of this study are available within the article.

REFERENCES

[1]F. Quin, M. Peng, D. Estevez, and C. Brosseau, "Electromagnetic composites: From effective medium theories to metamaterials," J. Appl. Phys. **132**, 101101 (2022).
[2]V. B. Bregar, "Effective-medium approach to the magnetic susceptibility of composites with ferromagnetic inclusions," Phys. Rev. B **71**, 174418 (2005).
[3]V. B. Bregar, "Advantages of ferromagnetic nanoparticle composites in microwave absorbers," IEEE Trans. Magn. **40**, 1679–1684 (2004).
[4]P. Barber, S. Balasubramanian, Y. Anguchamy, S. Gong, A. Wibowo, H. Gao, H. J. Ploehn, and H.-C. zur Loye, "Polymer composite and nanocomposite dielectric materials for pulse power energy storage," Materials **2**, 1697–1733 (2009).
[5]J. Helsing, J. Axell, and G. Grimvall, "Conduction in inhomogeneous materials: Hot and high-field spots," Phys. Rev. B **39**, 9231 (1989).
[6]Y. S. Li and P. M. Duxbury, "From moduli scaling to breakdown scaling: A moment-spectrum analysis," Phys. Rev. B **40**, 4889 (1989).
[7]K. R. Foster, M. C. Ziskin, Q. Balzano, and G. Bit-Babik, "Modeling tissue heating from exposure to radiofrequency energy and relevance of tissue heating to exposure limits: Heating factor," Health Phys. **115**, 295–307 (2018).
[8]S. Corovic, I. Lackovic, P. Sustaric, T. Sustar, T. Rodic, and D. Miklavcic, "Modeling of electric field distribution in tissues during electroporation," Biomed. Eng. Online **12**, 16 (2013).
[9]J. P. Calame, "Finite difference simulations of permittivity and electric field statistics in ceramic-polymer composites for capacitor applications," J. Appl. Phys. **99**, 084101 (2006).
[10]H. Cheng and S. Torquato, "Electric-field fluctuations in random dielectric composites," Phys. Rev. B **56**, 8060 (1997).
[11]D. Cule and S. Torquato, "Electric-field distribution in composite media," Phys. Rev. B **58**, R11829 (1998).
[12]M. Beran, "Field fluctuations in a two-phase random medium," J. Math. Phys. **21**, 2583–2585 (1980).
[13]J. Axell, "Bounds for field fluctuations in two-phase materials," J. Appl. Phys. **72**, 1217–1220 (1992).
[14]S. Torquato, *Random Heterogeneous Materials, Microstructure and Macroscopic Properties* (Springer, Berlin, 2002).
[15]G. W. Milton, *The Theory of Composites* (Cambridge University Press, Cambridge, 2002).
[16]A. Sihvola, *Electromagnetic Mixing Formulas and Applications* (Institution of Engineering and Technology, London, 1999).
[17]T. C. Choy, *Effective Medium Theory: Principles and Applications* (Oxford University Press, Oxford, 1999).
[18]In this alternative time-harmonic convention, $\mathbf{E}_{\text{hom}}(\mathbf{r}, t) \propto e^{i(k'z-\omega t+\phi)}$, with $\varepsilon_{\text{hom}} = \varepsilon'_{\text{hom}} + i\varepsilon''_{\text{hom}}$ and $k = k' + ik''$. The inequalities $k', k'', \varepsilon'_{\text{hom}}, \varepsilon''_{\text{hom}} \geq 0$ also hold for this convention.
[19]In the case of magnetic composites, the wave vector becomes $k_{\text{eff}} = (\omega/c)\sqrt{\varepsilon_{\text{eff}}\mu_{\text{eff}}}$, where μ_{eff} is the relative permeability. Then, the wave propagation corresponds to that in a homogeneous medium with $\varepsilon_{\text{hom}} = \varepsilon_{\text{eff}}$ and $\mu_{\text{hom}} = \mu_{\text{eff}}$. Apart from this, Eqs. (1)–(6) remain unchanged.

[20]J. Monecke, "Microstructure dependence of material properties of composites," Phys. Status Solidi B **154**, 805–813 (1989).
[21]G. Bánhegyi, "Comparison of electrical mixture rules for composites," Colloid Polym. Sci. **264**, 1030–1050 (1986).
[22]R. Pelster, "Bounds for local and average microwave absorption in heterogeneous systems," J. Colloid Interface Sci. **318**, 534–540 (2008).
[23]R. Pelster, B. Hallouet, and C. Volz, "Evaluation of a rigorous lower bound for the intrinsic conductivity of dispersed particles in composites with unknown microstructure," J. Phys. D: Appl. Phys. **48**, 145306 (2015).
[24]V. M. Shalaev, "Electromagnetic properties of small-particle composites," Phys. Rep. **272**, 61–137 (1996).
[25]B. Hallouet and R. Pelster, "3D-simulation of topology-induced changes of effective permeability and permittivity in composite materials," J. Nanomater. **2007**, 080814.
[26]R. Pelster, A. Spanoudaki, and T. Kruse, "Microstructure and effective properties of nanocomposites: Ferrofluids as tunable model systems," J. Phys. D: Appl. Phys. **37**, 307–317 (2004).
[27]R. Pelster, "Dielectric spectroscopy of confinement effects in polar materials," Phys. Rev. B **59**, 9214–9228 (1999).
[28]B. Hallouet, B. Wetzel, and R. Pelster, "On the dielectric and magnetic properties of nanocomposites," J. Nanomater. **2007**, 034527.
[29]B. Hallouet, P. Desclaux, B. Wetzel, A. K. Schlarb, and R. Pelster, "Analysing dielectric interphases in composites containing nano- and micro-particles," J. Phys. D: Appl. Phys. **42**, 064004 (2009).
[30]D. Shamoon, S. Lasquellec, and C. Brosseau, "Low-order statistics of effective permittivity and electric field fluctuations in two-phase heterostructures," J. Appl. Phys. **122**, 044106 (2017).
[31]K. Günther and D. Heinrich, "Dielektrizitätskonstante, Permeabilität, elektrische Leitfähigkeit, Wärmeleitfähigkeit und Diffusionskonstante von Gemischen mit kugelförmigen Teilchen (gitterförmige und statistische Anordnung)," Z. Phys. **185**, 345–374 (1965).
[32]D. R. McKenzie, R. C. McPhedran, and G. H. Derrick, "The conductivity of lattices of spheres. II. The body centred and face centred cubic lattices," Proc. R. Soc. London Ser. A **362**, 211–232 (1978).
[33]L. Fu, P. M. Macedo, and L. Resca, "Analytic approach to the interfacial polarization of heterogeneous systems," Phys. Rev. B **47**, 13818 (1993).
[34]L. Fu and L. Resca, "Electrical response of heterogeneous systems of clustered inclusions," Phys. Rev. B **47**, 16194 (1993).
[35]P. Monk, *Finite Element Methods for Maxwell's Equations* (Oxford University Press, New York, 2003).
[36]See https://www.ansys.com/de-de/products/electronics/ansys-electronics-desktop for "Ansys Electronics Desktop (AEDT)" (accessed April 17, 2024).
[37]P. Hammond, "Electric and magnetic images," Proc. Inst. Electr. Eng. Part C **107**, 306–313 (1960).
[38]For the volume of the composite placed in the waveguide, $V = dhb = b^3/4$ holds, since $h = d = b/2$ (see Fig. 3). Thus, the average volume per particle in a composite containing N_{inc} particles equals $s^3 = b^3/(4N_{\mathrm{inc}})$. The length s is also a measure of the mean particle distance, and it is smaller than the width b of the waveguide: $b/s = (4N_{\mathrm{inc}})^{1/3} > 1$ holds. We obtain $b/s \simeq 3.4$ for $N_{\mathrm{inc}} = 10$ and $b/s \simeq 9.3$ for $N_{\mathrm{inc}} = 200$, i.e., for the standard number of particles we use in our simulations.
[39]For magnetic samples of relative permeability μ_{eff}, the effective permittivity in Eq. (16) is to be replaced by the ratio $\varepsilon_{\mathrm{eff}}/\mu_{\mathrm{eff}}$.
[40]A. M. Nicolson and G. F. Ross, "Measurement of the intrinsic properties of materials by time-domain techniques," IEEE Trans. Instrum. Meas. **19**, 377–382 (1970).
[41]W. B. Weir, "Automatic measurement of complex dielectric constant and permeability at microwave frequencies," Proc. IEEE **62**, 33–36 (1974).
[42]J. Qi, H. Kettunen, H. Wallén, and A. Sihvola, "Different homogenization methods based on scattering parameters of dielectric-composite slabs," Radio Sci. **46**, RS0E08 (2011).
[43]A. Spanoudaki and R. Pelster, "Effective dielectric properties of composite materials: The dependence on the particle size distribution," Phys. Rev. B **64**, 064205 (2001).
[44]J. C. M. Garnett, "Colours in metal glasses and in metallic films," Philos. Trans. R. Soc. London Ser. A **203**, 385–420 (1904).
[45]J. C. M. Garnett, "Colours in metal glasses, in metallic films, and in metallic solutions II," Philos. Trans. R. Soc. London Ser. A **205**, 237–288 (1906).
[46]*Surface and Colloid Science*, edited by S. S. Dukhin and E. Matijević (Wiley-Interscience, New York, 1971).
[47]*Emulsion Science*, edited by P. Sherman (Academic Press, London, 1968).
[48]For the latter equality, see Eq. (10), and keep in mind that we consider loss-free materials and, thus, $\langle E_{\mathrm{norm}}, y(\mathbf{r})\rangle_i \in \mathbb{R}$ holds—see Eqs. (11) and (12).
[49]J. D. Jackson, *Classical Electrodynamics*, 2nd ed. (Wiley, New York, 1975).